

A HIGH-RESOLUTION STUDY OF LOCAL DIAGENETIC EFFECTS ON THE
GEOCHEMISTRY OF THE LATE ORDOVICIAN KOPE FORMATION

Evelyn S Becerra

Submitted to the faculty of the University Graduate School
in partial fulfillment of the requirements
for the degree
Master of Science
in the Department of Earth Sciences,
Indiana University

September 2022

Accepted by the Graduate Faculty of Indiana University, in partial fulfillment of the requirements for the degree of Master of Science.

Master's Thesis Committee

William P. Gilhooly III, PhD, Chair

Kathy Licht, PhD

Gabriel Filippelli, PhD

© 2022

Evelyn S Becerra

DEDICATION

Dedico mi tesis a mis padres y hermana- Heriberto Becerra, Aurelia Sosa, y Marlene Becerra. Gracias por todo el cariño, ánimo, y apoyo que me han dado en todos mis años de estudio.

Al fin si se pudo.

ACKNOWLEDGEMENT

I would first like to thank my advisor, Bill. This project bloomed into something unexpected, and was not possible without Bill's expertise, guidance, and creativity. The many hours we spent on zoom were so worth it- I am proud of the results.

I also wish to thank my committee members Kathy Licht and Gabe Filippelli. Both provided valuable perspectives that allowed us to think outside the (geochemist) box. I am also very grateful for their support outside of schoolwork.

This project would not have been possible without the support of Ben Dattilo at Purdue University Fort Wayne. Ben provided the drill cores used in this project, shared stratigraphic and fossil knowledge on the Kope formation, and was our field guide. This knowledge was crucial in our interpretations of the data. He also helped me find the coolest trilobite fossils ever.

Thank you to my lab group members and Project Seed student interns. Alice Bosco Santos helped get me started in the lab and was always happy to answer any questions. I am grateful for the discussions on data and methods, and friendship. A special thank you to Brooke Vander Pas, for the endless help via text and phone call that helped direct the discussion. I would not have a completed document without Brooke's help.

I must also thank the Druschel lab group, especially Martin, John, and Sarah. Martin Kurek and John Shukle spent hours of their time on R assistance (and taught me to drive in snow). Sarah assisted me in the tedious job of sampling drill cores.

I would like to express my deepest appreciation for Steve Bates, my lab supervisor and mentor while at UCR. Steve taught me excellent lab habits and the

analytical instrument skills that allowed me to seamlessly integrate into my master's program. He also believed in my ability to succeed in graduate school when I didn't think it was an option for me. I will forever be grateful for the lab and life skills I learned from him.

Lastly, I am deeply indebted to my dad, mom, sister, and partner Martin. I would not be here without their unconditional love and support.

Evelyn S. Becerra

A HIGH-RESOLUTION STUDY OF LOCAL DIAGENETIC EFFECTS ON THE
GEOCHEMISTRY OF THE LATE ORDOVICIAN KOPE FORMATION

The Ordovician (485-444 Ma) was a highly dynamic period, characterized by significant evolutionary and climatic change. Paleozoic fauna which evolved during the Great Ordovician Biodiversification Event (GOBE) populated extensive epicontinental seaways. Major sea level fluctuations during The Hirnantian glaciation are believed to have led to a mass extinction event at the End Ordovician. However, a reassessment of Early Paleozoic fossil assemblages suggests the onset of extinctions began in the mid-Katian, ~3 million years before the Hirnantian. The Kope formation, within the North American succession of the Katian, was deposited during the peak biodiversification of the GOBE at the point which a biological crisis begins. The well-studied series of interbedded shale and fossiliferous limestone beds, deposited within a shallow epeiric sea, provide ideal sedimentological and paleontological context to interpret sediment geochemistry recorded at the onset of a global mass extinction.

For a high-resolution section of the Kope, $\delta^{34}\text{S}_{\text{pyrite}}$ show an extraordinary range of variability, up to 64.5‰, with systematic oscillations throughout the core. The isotope signal represents a mix of pyrite formed at the time of deposition and during diagenesis. As sea levels fluctuated, the amount of sediment delivery influenced the connection of sediment porewaters to overlying seawater sulfate and the location of the sulfate reduction zone, which in turn, masked the primary signal. Reactive iron data suggest low oxygen concentrations in the water column, however fossil assemblages found throughout the Kope suggest otherwise. Changes in sedimentation can mask the water

column signal, so these data also capture an aggregate signal. $\delta^{15}\text{N}_{\text{bulk}}$ show an upsection decrease of 4.4‰, followed by a 3.4‰ increase. Though this excursion can be interpreted as a switch to increased denitrification in a low oxygen environment, the fossil record suggests the data capture localized diagenetic reactions that occur below an oxic water column.

Perturbations in the ocean-climate system is often based on the interpretation of stable isotope excursions, and although excursions are diagnostic of changes to biogeochemical cycles, they may not fully account for diagenetic reactions that mask primary signals. The results from the Kope demonstrate strong localized, not global, controls on the sediment geochemistry.

William P. Gilhooly III, PhD, Chair

Kathy Licht, PhD

Gabriel Filippelli, PhD

TABLE OF CONTENTS

LIST OF TABLES.....	x
LIST OF FIGURES.....	xi
LIST OF ABBREVIATIONS	xiv
INTRODUCTION.....	1
HYPOTHESES.....	6
Hypothesis 1	6
Hypothesis 2	6
BACKGROUND.....	8
Late-Ordovician Mass Extinction	8
Geologic Setting	10
The Kope Formation.....	11
METHODS.....	16
Sample Core Collection	16
Sequential Iron Extraction.....	17
Carbonate Isotopes	19
Organic Carbon Isotopes	20
Bulk Nitrogen Isotopes.....	20
Sulfur Isotopes and Sulfide Concentrations	21
Total Carbon (TC) and Total Inorganic Carbon (TIC).....	22
RESULTS.....	23
Total Inorganic Carbon (TIC) and Total Organic Carbon (TOC)	23
Organic Carbon Isotopes	25
Inorganic Carbon and Oxygen Isotopes	25
Sulfur Isotopes.....	27
Reactive Iron.....	29
Nitrogen.....	30
DISCUSSION.....	34
Carbon Cycling and Isotopes	35
Sulfur and Iron.....	37
Nitrogen Cycling and Isotopes in Marine Environments	46
CONCLUSION	55
APPENDICES.....	57
Appendix A.....	57
Appendix B.....	63
REFERENCES.....	69
CURRICULUM VITAE	

LIST OF TABLES

Table 1. Dominant species of nitrogen in different redox conditions, their inhibitions, and relative isotope fractionations.	49
--	----

LIST OF FIGURES

<p>Figure 1. (A). C- and N-isotope excursions in the Vinini Creek Formation, NV showing a 1‰ increase in $\delta^{15}\text{N}$. Modified from Shen et al., (2018). (B). Preliminary $\delta^{15}\text{N}$ and TN data, from Orazi, (2016), for a core section of the Kope formation showing a ~3‰ upsection increase in $\delta^{15}\text{N}$ and consistent decreases in TN with lithologic change. This section is much earlier in time than Vinini Creek.</p>	3
<p>Figure 2. Diversification of Paleozoic fauna (modified from Rasmussen et al., 2019 and Stigall et al., 2020). Peak biodiversification occurred within the early-mid-Katian (*).</p>	5
<p>Figure 3. Map of the paleogeography of Laurentia during the Late Ordovician. Red star indicates the location of this study area. Modified from Brett et al., (2020).</p>	11
<p>Figure 4. Stratigraphy of the Late Ordovician. This study focuses on the Snag Creek and Alexandria sub-members of the Kope formation. Modified from Brett et al., (2008a).</p>	12
<p>Figure 5. Biostratigraphy, sequence stratigraphy, and C-isotope chemostratigraphy of the Katian of the Cincinnati Arch region. Modified from Brett et al., (2020). The symbol “*” indicates the beginning of decline in biodiversity as shown in Figure 2. The shaded region represents portion of the Kope sampled for this study.</p>	15
<p>Figure 6. Core extraction location (red star) in Boone County, KY.</p>	17
<p>Figure 7. Iron-speciation parameters for evaluating ocean redox conditions. Modified from Poulton and Canfield (2011).</p>	18
<p>Figure 8. Downcore concentrations and C-isotope compositions total inorganic carbon and total organic carbon.</p>	24
<p>Figure 9. Boxplot of $\delta^{13}\text{C}_{\text{org}}$ data grouped by lithology. Limestone average is -29.3‰, n=15. Mix average is -29.8‰, n=6. Shale average is -29.6‰, n=109.</p>	25
<p>Figure 10. (a) Scatter plot of $\delta^{13}\text{C}_{\text{carbonate}}$ and $\delta^{18}\text{O}_{\text{carbonate}}$ by lithology showing no correlation. (b) Boxplot of $\delta^{13}\text{C}_{\text{carbonate}}$ data grouped by lithology. Limestone average is -1.6‰, n=14. Mix average is -1.2‰, n=6. Shale average is -1.2‰, n=106.</p>	26
<p>Figure 11. Downcore S-isotope composition of pyrite, reactive iron, and N-isotope composition of total nitrogen.</p>	28

Figure 12. Boxplot of $\delta^{34}\text{S}$ grouped by lithology. Limestone average is -0.2‰ , $n=10$. Mix average is -8.3‰ , $n=6$. Shale average is 4.2‰ , $n=102$	29
Figure 13. (a) Scatterplot of TOC and TN showing no correlation. (b) Scatterplot of TOC and TN with shale, mix, and limestone lithologies showing no correlation. (c) Scatter plot of TOC/TC and TN showing strong correlation. P-value is <0.05 and adjusted r^2 is 0.4942. (d) Scatter plot of TOC/TC and TN with shale, mix, and limestone lithologies. Shale P-value is <0.05 and adjusted r^2 is 0.3374. Mix and limestone lithologies do not show good correlation due to small sample size. (e) Scatter plot of Al and TN showing strong correlation. P-value is <0.05 and adjusted r^2 is 0.8414. (f) Scatter plot of Al and TN with shale, mix, and limestone lithologies. Shale P-value is <0.05 and adjusted r^2 is 0.7489. Mix P-value is <0.05 and adjusted r^2 is 0.9819. Limestone P-value is <0.05 and adjusted r^2 is 0.7246.....	31
Figure 14. (a) Scatter plot of TIC and $\delta^{15}\text{N}_{\text{bulk}}$ showing no correlation. (b) Scatter plot of TIC and $\delta^{15}\text{N}_{\text{bulk}}$ with limestone, mix, and shale lithologies also show no correlation. (c) Scatter plot of C/N and $\delta^{15}\text{N}_{\text{bulk}}$ showing no correlation. (d) Scatter plot of C/N and $\delta^{15}\text{N}_{\text{bulk}}$ with limestone, mix, and shale lithologies also showing no correlation. (e) Scatter plot of Al and $\delta^{15}\text{N}_{\text{bulk}}$ do not show correlation. (f) Scatter plot of Al and $\delta^{15}\text{N}_{\text{bulk}}$ with limestone, mix, and shale lithologies also showing no correlation.....	32
Figure 15. Boxplot of $\delta^{15}\text{N}_{\text{bulk}}$ grouped by lithology. Limestone average is 3.0‰ , $n=12$. Mix average is 3.9‰ , $n=6$. Shale average is 3.8‰ , $n=107$	33
Figure 16. Downcore variation in the S-isotope composition of pyrite. The isotopic composition of Ordovician seawater sulfate (approximately 24‰ ; Kampschulte and Strauss, 2004) is indicated by the dashed line.....	39
Figure 17. Relationship between sediment accumulation rates and sea level change. Bars show position of SRZ (sulfate-reduction zone), RPD (redox-potential discontinuity) and SWI (sediment–water interface) at different stages of a sea level cycle. From Brett et al., (2008b).	43
Figure 18. Scatter plot of $\text{Fe}_{\text{HR}}/\text{Fe}_{\text{T}}$ and $\text{Fe}_{\text{py}}/\text{Fe}_{\text{HR}}$ showing the distribution of redox conditions of samples based on lithology.....	45
Figure 19. Cross plots of aluminum and each reactive iron species and the corresponding sample lithologies. Al vs Fe_{T} plots show a line with a slope of 0.66 which denote the threshold at which samples are considered to have authigenic iron enrichment.	46

Figure 20. Major chemical forms and transformations of nitrogen in the marine environment and their oxidation states. The color of the arrows denotes the redox condition: blue = oxic, purple = suboxic, and red = anoxic. *Assimilation and Ammonification can occur in both oxic and anoxic environments. Modified from Gruber, (2008).....47

Figure 21. Relationship between oxygen concentrations and N-isotope values and their associated species of nitrogen in the nitrogen cycle. Modified from Quan et al., (2013).51

LIST OF ABBREVIATIONS

C-isotope- Carbon isotope

GOBE- Great Ordovician Biodiversification Event

Fe_{carb}- Carbonate iron

Fe_{HR}- Highly reactive iron

Fe_{ox}- Iron oxides

Fe_{mag}- Magnetite iron

Fe_{py}- Pyrite iron

ICP-OES- Inductively coupled plasma optical emission spectroscopy

IRMS- Isotope ratio mass spectrometer

N-isotope- Nitrogen isotope

N-fixation- Nitrogen fixation

O-isotope- Oxygen isotope

S-isotope- Sulfur isotope

SRZ- Sulfate reduction zone

INTRODUCTION

The Ordovician (485-444 Ma) was a highly dynamic geologic period, characterized by both significant evolutionary and climatic change. During the Great Ordovician Biodiversification Event (GOBE), the number of marine families tripled as new benthic fauna (brachiopods and echinoderms) replaced Cambrian fauna (Bottjer et al., 2001; Sepkoski, 1981; Servais et al., 2010; Webby et al., 2012). Concurrent with this event was a rise in atmospheric oxygen. A doubling of concentrations from 12% during the Middle Ordovician to 25% during peak diversification in the Late Ordovician is believed to have played a significant role during the GOBE (Edwards et al., 2017; Stigall, 2017). The new Paleozoic faunas primarily populated the broad and extensive shallow seaways on continental margins. Unlike modern shelf environments, these shallow seaways had broad gentle slopes that extended for kilometers (e.g., Dattilo et al., 2008b). Small changes in sea levels thus greatly impacted the position of the shoreline, and therefore faunal habitat, as well as the location of sediment deposition (Brett et al., 2008b; Brett et al., 2020).

Although the shallow sea environment was dynamic, the long periods of faunal stability suggest some level of ecological resilience. However, as rapidly as metazoans radiated and diversified, the Ordovician abruptly ended with a biological crisis when 85% of marine species went extinct during a major mass extinction event (Jablonski, 1991). The End Ordovician mass extinction is thought to have been caused by the Hirnantian glaciation, which dramatically switched the Ordovician climate from a “hot house” with elevated CO₂ levels, to an “ice house” with decreased CO₂ (Brenchley 1984). The drop in sea level associated with glaciation removed critical shallow shelf habitat, which created

physical environmental stress that contributed to mass extinction (Brenchley 1984; Sheehan, 2001). Furthermore, there is evidence that oxygen deficiency in some areas of the Ordovician ocean may have led to ferruginous to euxinic conditions, which may have contributed to the extensive loss of marine life at the End Ordovician (Zou et al., 2018). Causes for the Hirnantian glaciation remain poorly understood, though hypotheses include changes in carbon cycling, increased silicate weathering, changes in albedo due to volcanism, increased influx in extraterrestrial metals, or a combination of factors (Brenchley et al., 2003; Buggisch et al., 2010; Kump and Arthur, 1999; Reiners and Turchyn, 2018).

One possible reason for these different interpretations may be associated with the complexity of the geochemical record retained in Ordovician sedimentary sequences. My overarching research question is about the ways in which the process of sedimentation affects the geochemical record. Most studies of carbon isotope (C-isotope) excursions in the Ordovician assume that mountain building events and climatic changes during this period drastically altered the chemistry of the ancient oceans throughout the world (e.g., Pancost et al., 2013). However, my investigations into the nitrogen isotope (N-isotope) and sulfur isotope (S-isotope) variability suggest these isotope systematics were influenced by localized effects (rather than global) that were sensitive to relatively shorter time scale perturbations.

For example, an N-isotope study of the Hirnantian (Figure 1A) observed a large positive isotope excursion through the end Ordovician to early Silurian (Shen et al., 2018). The authors attribute the 1‰ increase in N-isotope values to a change in the ecology of primary producers. They proposed a switch from cyanobacteria to relatively

larger picoplankton, with higher settling velocities that could have enhanced carbon burial and resulted in a positive C-isotope excursion in the Hirnantian. Under the scenario of Shen et al. (2018), the increased CO₂ drawdown from greater settling velocities, and therefore increased carbon burial, created the global cooling necessary for glaciation that triggered the mass extinction.

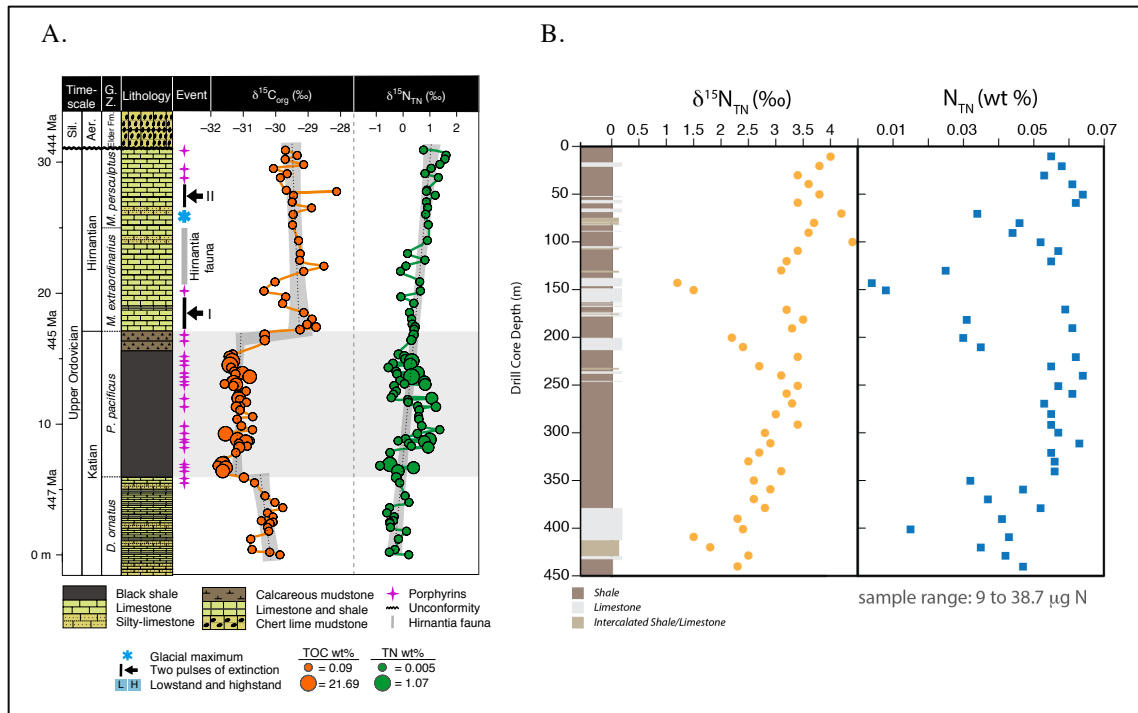


Figure 1. (A). C- and N-isotope excursions in the Vinini Creek Formation, NV showing a 1‰ increase in δ¹⁵N. Modified from Shen et al., (2018). (B). Preliminary δ¹⁵N and TN data, from Orazi (2016), for a core section of the Kope formation showing a ~3‰ upsection increase in δ¹⁵N and consistent decreases in TN with lithologic change. This section is much earlier in time than Vinini Creek.

While the Shen et al. (2018) N-isotope excursion is significant, preliminary data (Figure 1B) for the Kope formation show a much greater variability in N-isotope compositions (~3‰) measured at a higher sampling resolution and within a smaller section of drill core (Orazi et al., 2016) that occurred at least 3 million years prior to the Hirnantian (Brett et al. 2020; Ellwood et al., 2007). Evaluating the range of isotopic variability and the processes that produced these signatures therefore has important

implications for contextualizing the environmental conditions that existed before the extinction event.

Similar observations in the S-isotope variability of pyrite have been made in recent studies that suggest localized effects play a significant role in the S-isotope record. Liu et al. (2019) propose switches between high and low sedimentation rates create an “open” or “restricted” exchange of sulfate between porewaters and the overlying seawater, which create oscillations in S-isotope values due to the changes in sulfur fractionation during formation of pyrite. Pasquier et al. (2017) attribute changes in S-isotope values to sea level oscillations during glacial-interglacial periods over the last 500 ky in the northwestern Mediterranean basin. Within the context of the Ordovician, Marshall (2011) discusses the use of S-isotopes in the Kope formation as a proxy for sedimentation rate. Collectively these studies suggest that the diagenetic component to sulfur cycling may have a significant impact on the S-isotope composition preserved in sedimentary archives.

Though several studies document long time-scale changes in geochemistry throughout the Ordovician, there is currently a lack of high-resolution geochemical data that match the frequency of sea level fluctuation observed in the lithological record (Miller et al., 2005). Such a record can elicit more nuanced interpretations about the Late Ordovician biosphere prior to the Hirnantian glaciation. An improvement to the record through an approach such as this could perhaps sharpen the interpretations of possible triggers of biotic crises that occurred toward the end of the Ordovician.

A section of the Kope formation was selected for this study because it is comprised of well-studied, correlated, and recognizable marker beds and biostratigraphy

that make 10 meter-scale cycles easily identifiable. Moreover, a recent reassessment of fossil assemblages of the Early Paleozoic suggests the onset of extinctions in the Late Ordovician began in the mid-Katian, at least 3 million years before the Hirnantian (Brett et al., 2020; Ellwood et al., 2007; Rasmussen et al., 2019). This section of the Kope was deposited during the peak biodiversification of the GOBE (Figure 2), at the tipping point at which a biological crisis interval (Rasmussen et al., 2019) and a major decline in atmospheric oxygen begins (Edwards et al., 2017).

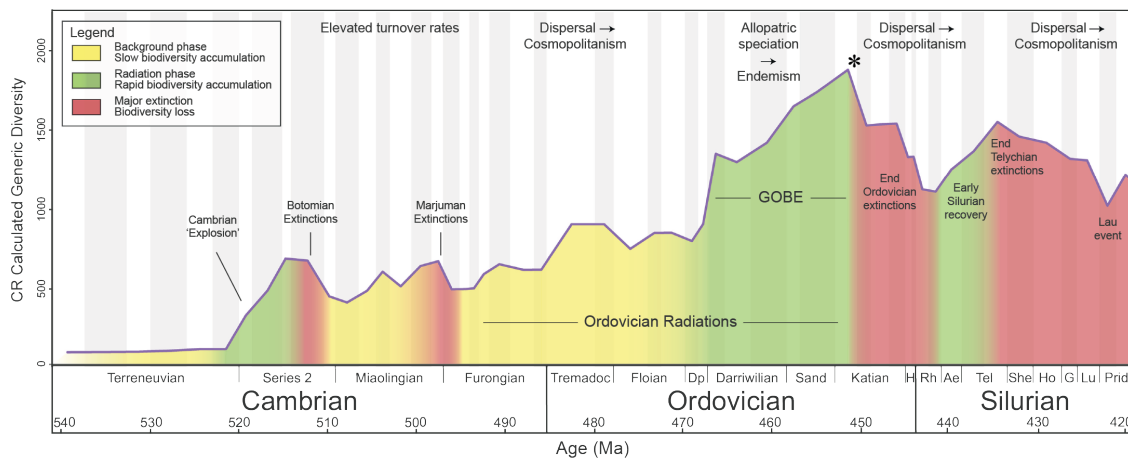


Figure 2. Diversification of Paleozoic fauna (modified from Rasmussen et al., 2019 and Stigall et al., 2020). Peak biodiversification occurred within the early-mid-Katian (*).

This study uses baseline behavior and variation in isotope geochemistry within the Kope formation, which have not yet been documented, to contribute to ongoing critical questions regarding the GOBE including (Stigall et al., 2020): 1) What is the relationship between local and global trends? and 2) Which of the many environmental changes facilitated diversification and which were truly initiating factors?

HYPOTHESES

Hypothesis 1

I hypothesize localized changes in sedimentation rates, caused by changes in sea level, should affect the S-isotope composition of sedimentary pyrite in this section of the Kope formation. Recent studies have demonstrated that pyrite S-isotope values in marine sediments are responsive to sedimentation rate. Liu et al. (2019) observed a pattern of increased and high S-isotope values in pyrite that approached the isotopic composition of seawater sulfate during periods of rapid sedimentation in Pleistocene sediments from the East China Sea. Those S-isotope values of pyrite also decreased during periods of low sedimentation rates. Richardson et al. (2019) observed a similar pattern in Silurian-aged sediments. S-isotope values in pyrite were higher and more variable in sediments from shallow water facies, and low and invariant in deep water facies. Furthermore, S-isotope analyses on the Alexandria sub-member of the Kope formation show $\delta^{34}\text{S}$ values in pyrite are consistently low in limestones relative to those in shale (Marshall, 2011). Their sampling strategy focused on collecting thick limestone beds and the shale between these beds; however, my field observations of the Kope indicate a far greater lithologic change than represented by this approach. I anticipate that including the thinner limestone beds will provide a more representative view of S-isotope variability within the Kope formation.

Hypothesis 2

I hypothesize that sea level change influences nitrogen cycling and therefore the N-isotope retained in the sedimentary record. Pyrite sulfur burial and the sulfate reduction rates that drive the production of pyrite, are in part controlled by the

availability of organic matter in the system. Also dependent on organic matter are the three main reactions that occur in the nitrogen cycle: nitrification, denitrification, and nitrogen fixation. So, if there are significant changes in pyrite S-isotopes, caused by sea level fluctuations, those changes likely influence the nitrogen cycle and therefore the N-isotope retained in the sedimentary record.

Preliminary data lend support to the hypothesis that N-isotopes in the Kope formation can be revealed through high-resolution sampling analysis (Figure 1B). Data show an overall positive increase in N-isotope values up-section. Shen et al. (2018) argue that a 1‰ increase in N-isotopes observed in the relatively deeper water Vinini Creek formation is associated with a significant change in primary productivity (Figure 1A). Increased primary productivity enhanced CO₂ drawdown and caused a cooling event that resulted in a glaciation. In comparison, initial N-isotope data from the Kope formation records a 3‰ increase that occurred earlier in time. Closer inspection of the preliminary data also reveals there are systematic decreases in the N-isotope signature within the carbonates (Figure 1B). These preliminary data suggest there are other controls on the N-isotope signatures in addition to primary productivity.

BACKGROUND

Late-Ordovician Mass Extinction

The Ordovician was an especially important time for the early evolution of animal life. The geologic period began with rapid radiation and diversification of metazoans during the Great Ordovician Biodiversification Event (GOBE) and abruptly ended with a global mass extinction event (Jablonski, 1991). Biodiversity began to decline through a series of step-changes beginning in the middle Katian (Figure 2) with the overall extinction culminating in the Hirnantian Age to the Rhuddanian Age of the Early Silurian (445.2-443.8 Ma) that resulted in the loss of 85% of marine species (Sheehan et al., 2001). The glaciation was a result of the intensified drawdown of atmospheric CO₂, which altered the Greenhouse Effect, allowed heat to be lost to space, and expanded glacial coverage. The dramatic switch from a “hothouse” to “icehouse” was detrimental to marine biota adapted to intense greenhouse conditions. Water trapped in ice caps decreased sea level, drained epeiric seaways, and removed critical habitat for marine life (Brenchley et al., 2003; Sheehan, 2001).

The environmental conditions during the Ordovician differed greatly to those today. Throughout the Ordovician atmospheric CO₂ levels were 16 times the present atmospheric levels (PAL) (Sheehan, 2001). However, greenhouse gasses compensated for the sun’s luminosity at 95.5% of present levels (Bernier, 1994; Kasting, 1992; Sheehan, 2001). Warmer climate and higher sea levels during the Ordovician flooded continents and created epeiric seaways that extended for kilometers. These broad platforms were widespread and acted as shallow water habitat for benthic fauna including brachiopods, crinoids, trilobites, and bryozoans among others.

Extensive glaciation during the Hirnantian centered on the supercontinent Gondwana, which was positioned over the southern pole (Brenchley et al., 1994). The expansion and contraction of the glaciers are associated with two pulses of extinction (Harper et al., 2014). The first pulse is associated with the initial change in climate and a drop in sea level. This increased ocean circulation, removed critical shallow shelf habitat, and created environmental stress (Brenchley 1994; Sheehan, 2001). During this period, shallow-water and deep-water fauna were the most affected through intermittent or weak euxinia (Sheehan, 2001; Zou et al., 2018). A second pulse of extinction occurred during an interval of rapid sea level rise and return to pre-glacial conditions. During this pulse, ocean circulation became sluggish and subsequent widespread anoxia and euxinia killed off many of the surviving taxa from the first pulse (Melchin et al., 2013; Sheehan, 2001; Zou et al., 2018). In total 26% of families, 49% of genera, and 85% of marine species went extinct (Jablonski, 1991; Sepkoski, 1996; Sheehan, 2001).

The causes for the Hirnantian glaciation remain poorly understood, but there are currently several different hypotheses that attempt to explain the drivers: 1) increased silicate weathering during the Taconic Orogeny caused a long-term decrease in CO₂ and perpetuated positive feedbacks that resulted in the growth of ice sheets until weathering rates declined (Kump et al., 1999); 2) increased albedo due to volcanic release of SO₂ that resulted in climatic cooling and formation of ice sheets (Buggisch et al., 2010); 3) changes in C- and O-isotope data from biogenic carbonate show a relationship between the onset of the glaciation and changes in the carbon cycle (Brenchley et al., 2003); 4) extra-terrestrial dust rich in metals fertilized oceans, increased marine productivity, and increased drawdown of CO₂ resulting in a glaciation event (Reiners et al., 2018); 5)

volcanogenic greenhouse gases caused warming around the Katian-Hirnantian boundary that led to expansion of preexisting deep water oxygen minimum zones, productivity collapse, and the first Late Ordovician mass extinction pulse (Bond and Grasby, 2020); or a combination of these factors (Harper et al., 2014).

Geologic Setting

The Cincinnatian series, the North American succession within the Katian Age (452-445.2 Ma), exhibits regular cycles of mudstone and limestone beds on the order of 1 and 10-meters thick, and are thought to be representative of the cyclicity in depositional environment during sea level fluctuations. The Cincinnati region was located on the continent of Laurentia in a deep subtidal environment within an epeiric sea with maximum depths of 40 meters (Figure 3; Brett et al., 2020; Datillo et al., 2008). The study area was positioned at $\sim 20^\circ$ south of the paleoequator and rotated 45° from its current position within a warm and tropical climate. Sedimentary structures, such as ripples with large wavelengths and locations of amalgamated and non-amalgamated fossil shells deposited during the Ordovician, suggest this position would have been prone to severe storms such as hurricanes (Brett et al., 2008b; Jin et al., 2013). The climate dynamics that promote hurricane formation in the tropics during the late Ordovician were similar to present day conditions due to the presence of ice caps in the south pole and steep temperature gradients between polar and tropical areas (Jin et al., 2013).

East of the Cincinnati region, active tectonic activity from the uplift of the Taconic Mountains caused high sediment input. The Taconic Orogeny occurred in three phases as different island arcs were accreted onto Laurentia (Cocks and Torsvik, 2011). The third phase of the orogeny occurred 453-443 Ma during the Katian to the Hirnantian.

The Taconic Foreland basin acted as a barrier that prevented sediment deposition on carbonate platforms. During high sedimentation periods, however, the Taconic Mountains deposited large amounts of siliciclastic sediment onto this area through the Sebree trough.

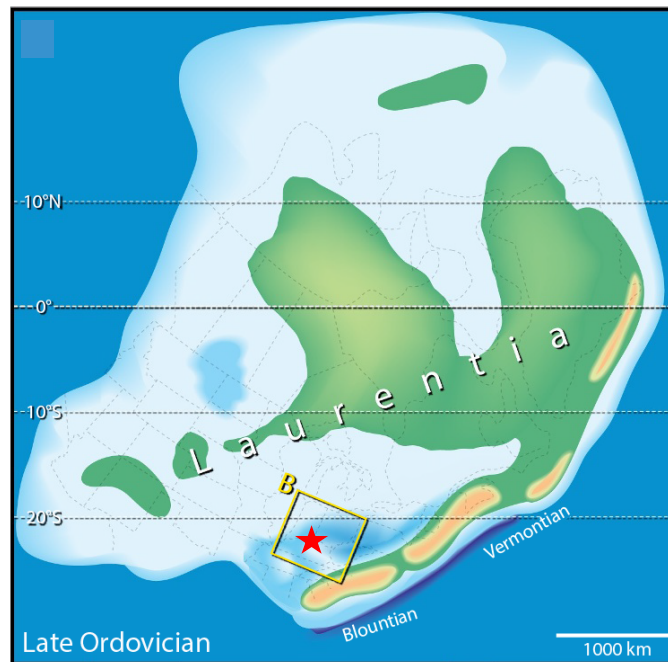


Figure 3. Map of the paleogeography of Laurentia during the Late Ordovician. Red star indicates the location of this study area. Modified from Brett et al., (2020).

The Kope Formation

The Kope formation, deposited within the upper Ordovician Cincinnati series, contains a series of interbedded mudstone and fossiliferous limestone beds deposited within a shallow epeiric sea (Brett et al., 2008a, Brett et al., 2008b; Holland et al., 1997; Holland et al., 2001; Jennette and Pryor, 1993). The formation is a ~70-meter thick unit that extends through southern Indiana, southwestern Ohio, and northern Kentucky. It represents the distal facies of a shallow, northward-dipping carbonate ramp consisting of the Kope, Fairview, and Grant Lake formations (Jeannette and Pryor, 1993; Miller et al., 1997). The depositional setting was a low energy environment, below wave base, that

was only affected by the strongest storms (Holland et al., 1997). The Kope formation is divided into three members and further divided into six sub-members (Figure 4). This study focuses on the Southgate member and the Snag Creek and Alexandria sub-members within the Kope formation.

SYSTEM	SERIES	STAGE	FORMATION	MEMBER	SUB MEMBER
ORDOVICIAN	CINCINNATIAN	MAYSVILLIAN (PART)	GRANT LAKE	Mt. AUBURN	
				CORRYVILLE	
				BELLEVUE	
			FAIRVIEW	FAIRMOUNT	
				Mt. HOPE	
		EDENIAN	KOPE	McMICKEN	Taylor Mill
					Grand Avenue
				SOUTHGATE	Grand View
					Alexandria
		Snag Creek			
	ECONOMY	Pioneer Valley			
		Brent			
	MOWHAWKIAN (PART)	SHERMANIAN		Pt. PLEASANT	Fulton
				BROMLEY	

Figure 4. Stratigraphy of the Late Ordovician. This study focuses on the Snag Creek and Alexandria sub-members of the Kope formation. Modified from Brett et al., (2008a).

The interbedded mudstone and fossiliferous limestone beds have cyclical patterns of deposition tied to sea level change. Their alternations are thought to have formed during millennial-scale periods of alternating siliciclastic sediment starvation combined with episodes of storm-related reworking and winnowing (Brett et al., 2008b; Holland et al., 1997; Jennette and Pryor, 1993). Mudrock intervals represent “time poor” deposits of

abrupt and episodically emplaced event beds. Though mudstones would appear to be quiet accumulations of sediment below wave base, upon closer look this is not the case. Siltstone beds (within mudstones) show sedimentary structures indicative of turbulence and scouring, such as tool marks, hummocky cross-stratification, grading, and other high energy sedimentary features (Brett et al., 2008b). Furthermore, well preserved fauna are frequently found in living position, indicating the organisms were buried in place by rapid deposition (e.g. Brett et al., 2008a; Brett et al., 2008b). The consistent evidence for rapid burial suggests the mudstones represent relatively short intervals of time since the thickness of the mudstones was an accumulation of single rapid burial events possibly caused by turbidity currents, hurricanes, or tsunamis (Brett et al., 2008a). Fossiliferous limestone beds on the other hand, represent “time rich” deposits of repeated storm winnowing and reworking of shell debris during low sedimentation (Brett et al., 2008a). Shell beds are usually indicative of large events that produce high sedimentation and reworking; however, sedimentary structures show this is not true. Concretions found in these beds suggest inhibition of sedimentation since concretions need time to indurate and cement. Low sedimentation rates also allowed colonization of highly diverse benthic organisms on the seafloor and the formation of shell beds. Large storms during these periods would rework and further concentrate skeletal material.

Mudstone and limestones within the Kope repeat in near-regular cycles in 1-meter and 10-meter scale cycles. These sediment packages can have widely different thicknesses implying they operated on different time scales. Meter-thick cycles, the smallest of these units, consist of alternating intervals of 0.3 to 3.0-meter thick mudstone beds sandwiched between limestone beds that can be laterally correlated at regional

scales (Brett et al., 2008; Holland et al., 2000). In the field they are identified as abrupt increases in thickness of shale beds (Holland et al., 1997). There are different interpretations on the mechanisms for the formation of meter-scale cycles. Proposed explanations include fluctuation in sea level controlled by glacier ice volume, change in deposition of proximal to distal storm beds, and changes in siliciclastic input (Elwood et al., 2007; Holland et al., 1997; Jeannette and Pryor, 1993). Superimposed on this are 10-meter scale cycles, which are groups of typically four or five meter-scale cycles (Brett et al., 2008a). About 30-70% of 10-meter cycles consist of grouped limestone beds, which represent the caps of meter cycles (Brett et al., 2008a). Using the carefully documented lithology and fossil assemblages of cycles, the Kope formation has the advantage of being easily identified in the field and in the drill core selected for this study.

The one-meter cycles of mudstone and limestone are recognized as 5th order sequences, or the smallest scale and highest frequency cycles, and represent tens of kyr (Brett et al., 2008a; Brett et al., 2008b). These were numbered 1-47 according to Holland et al. (1997) and are usually followed by “big shale” beds. These shale beds are recognized as 4th order cycles, which represent 100-400 kyr (Brett et al., 2020). These cycles, as well as C-isotope excursions, lithology, and biostratigraphy from this area are well studied and have been correlated across local regions, where individual beds and fossil events have been traced throughout Indiana, Kentucky, and Ohio (Figure 5). Moreover, the C-isotope excursions in these rocks record perturbations that have been identified locally and correlated globally between records in the U.S., Estonia, China, Canada, etc. (Bergström et al., 2010; Brett and Algeo, 2001; Jones et al., 2011; Young et al., 2008).

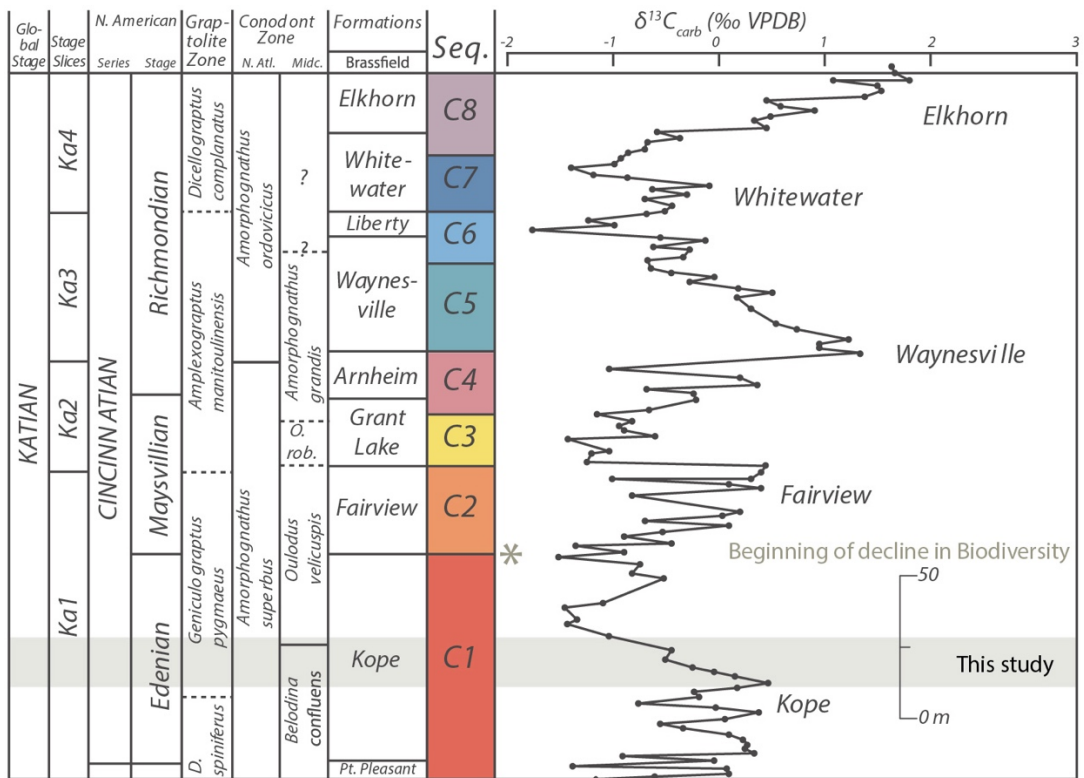


Figure 5. Biostratigraphy, sequence stratigraphy, and C-isotope chemostratigraphy of the Katian of the Cincinnati Arch region. Modified from Brett et al., (2020). The symbol “*” indicates the beginning of decline in biodiversity as shown in Figure 2. The shaded region represents portion of the Kope sampled for this study.

METHODS

Sample Core Collection

Samples were collected from a drill core archive and provided by collaborator Dr. Benjamin Dattilo at Purdue University Fort Wayne, IN. Drill core samples are less likely to be altered during post-depositional diagenesis, making it ideal for geochemical analyses. Thin sections that were made from different depths in the core show well preserved fossils and minimal alteration from meteoric water. This suggests minimal alteration to the chemical signatures used in this study. The drill core was extracted in Boone County, KY southwest of Cincinnati, OH as part of the Kenton County conveyance tunnel construction (Figure 6). Drilling began ~4.5 meters below ground level, with a total of 91 meters of recovery. The core was then divided into 4.5 meters increments and stored in sample core Box 1-21, Box 1 being the youngest. This study focuses on Boxes 15-17 (65.61 – 78.62 meters in depth), which encompass a section of the Kope formation. Core sections were sampled every ~10 cm for a total of 131 powdered samples. Each sample has been classified by lithology as limestone, mix, or shale.

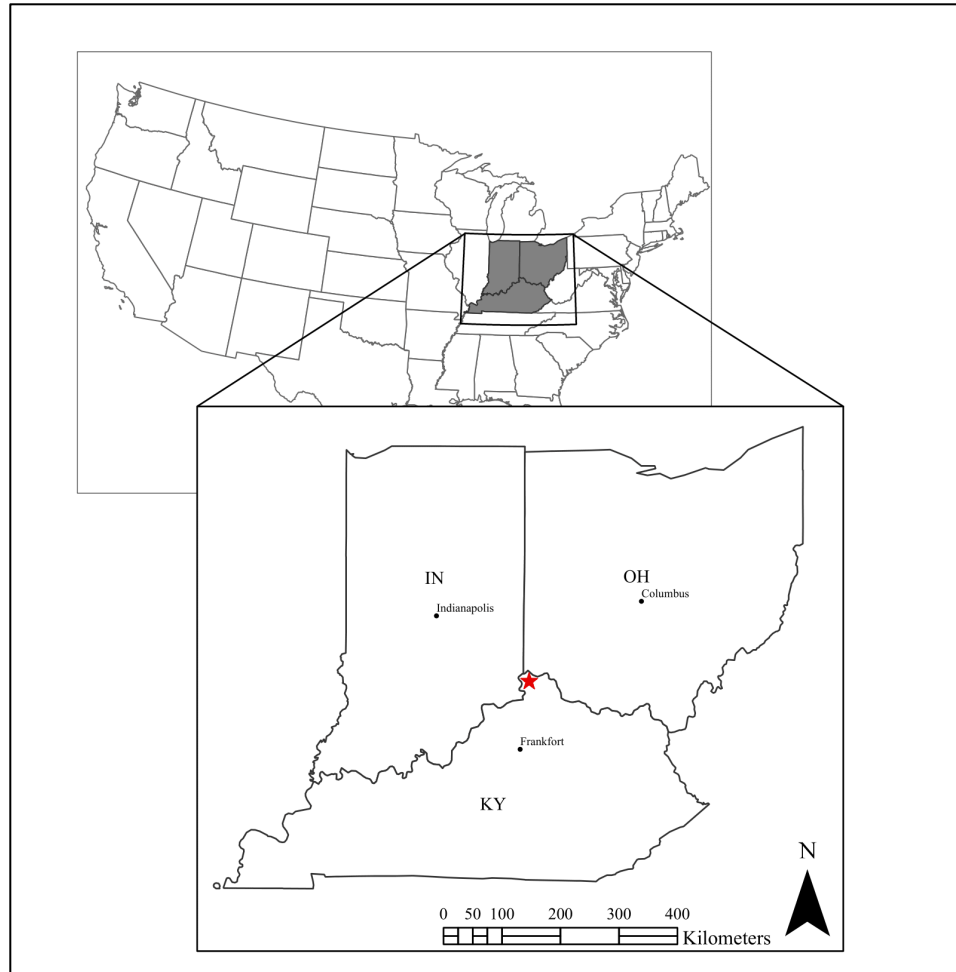


Figure 6. Core extraction location (red star) in Boone County, KY.

Sequential Iron Extraction

Iron minerals were extracted to develop a record of oxygen availability throughout the sediment record in Boxes 15-17. This proxy characterizes the relative distribution of highly reactive iron minerals that can be used to determine the mobility of iron which, in turn, can be used as proxy evidence for the redox conditions in the water column at the time of sediment deposition (e.g., Poulton and Canfield, 2011). Highly reactive iron (Fe_{HR}) is composed of iron carbonates (Fe_{carb} ; siderite and ankerite), ferric(oxyhy)droxides (Fe_{ox} ; ferrihydrite, lepidocrocite, goethite, and hematite), magnetite (Fe_{mag}), and sulfide (Fe_{py} ; pyrite), where $Fe_{HR} = Fe_{carb} + Fe_{ox} + Fe_{mag} + Fe_{py}$. Iron

deposited in oxic water columns will result in a Fe_{HR}/Fe_T ratio that does not exceed 0.38 (Figure 7). Values greater than 0.38 are found in anoxic conditions. If the water column is anoxic, the Fe_{py}/Fe_T ratio is additionally used to determine ferruginous or euxinic conditions. Ferruginous conditions occur when Fe(II) is mobilized in an anoxic and non-sulfidic water column. Euxinic conditions, on the other hand, are caused by an increased amount of H_2S (hydrogen sulfide) in an anoxic water column. These two conditions are determined by the extent of pyritization in the highly reactive pool (Poulton and Canfield, 2011). A Fe_{py}/Fe_{HR} ratio value above 0.8 suggests euxinic conditions while below this value suggests ferruginous (Figure 7).

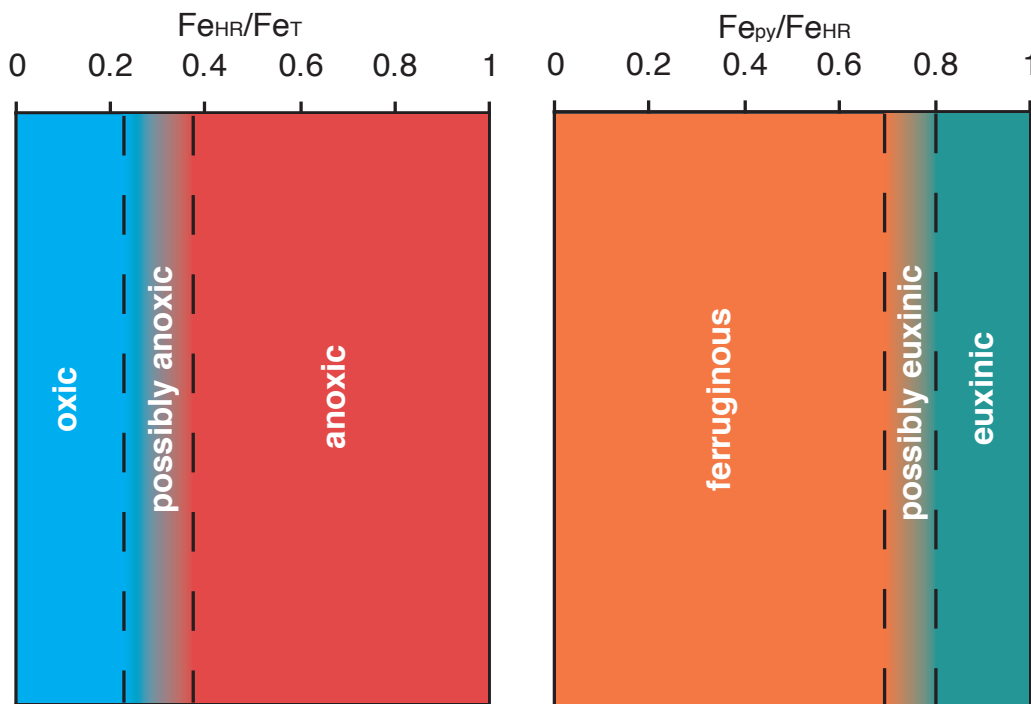


Figure 7. Iron-speciation parameters for evaluating ocean redox conditions. Modified from Poulton and Canfield (2011).

Iron carbonates, ferric(oxyhydroxides), and magnetite mineral phases were extracted by sequential reactions according to the method by Poulton and Canfield (2005). In this method, ~100 mg of rock sample powder are reacted with sodium acetate

at a pH of 4.5 for 48 hours, sodium dithionite at a pH of 4.8 for 2 hours, and ammonium oxalate at a pH of 3.2 for 6 hours. Aliquots of sample are taken from supernatant after centrifuging samples immediately after each reaction step. Sample concentrations were measured using ICP-OES. To extract total iron (Fe_T), 100 mg of sample powder were digested using 6N HCl in a CEM MDS 2000 microwave. Concentrations were measured on a Perkin Elmer ICP-OES.

Carbonate Isotopes

Carbonate C-isotope excursions for the Ordovician are well studied and correlated both locally and globally and can be used as a proxy for primary productivity in the ocean (Bergstrom et al., 2010; Kump and Arthur 1999). A positive excursion is attributed to an increase in organic carbon burial while a negative excursion results from reduced primary production of organic matter (Kump and Arthur 1999). The isotope value will reflect the value of the dissolved inorganic carbon pool of the water column. In this study isotope values will be used to correlate to the preexisting C-isotope record to determine how much time is represented in the core as well as where in time they are located.

To determine C-isotope ratios of carbonate in these samples, 0.15-7 mg of sample were weighed into glass vials, acidified with concentrated phosphoric acid (H_2PO_4), and heated for 1 hour at 72°C. Sample gas was analyzed by an injection needle on a Gasbench II coupled to a Delta V isotope ratio mass spectrometer (IRMS) in continuous flow mode. Samples were corrected to VPDB standards: NBS-18 (-5.014 ‰), NBS-19 (1.95‰), and IAEA-C09 (-47.321‰). Precision based on replicate sample measurements was within 0.1‰ (1σ).

Organic Carbon Isotopes

Organic C-isotopes can also be used as a proxy for productivity and burial in the ocean during the Ordovician. Organic C-isotopes will reflect the isotope composition of primary producers that utilize dissolved carbon. An increase in productivity and carbon burial will result in an increase in organic C-isotopes (Kump and Arthur, 1999).

Moreover, an increase in burial of organic carbon results in a decrease of pCO₂ which can have implications for the Ordovician climate (Kump and Arthur, 1999). Organic C-isotopes can also be utilized to determine diagenetic alteration. Covariance between the C-isotopes of organic carbon and carbonate indicate minimal diagenetic alteration and that these phases have retained their original isotopic values (Oehlert and Swart, 2014).

To determine isotope values, 10 mg of sample were weighed into pressed silver cups and acidified by fuming with an open beaker of 80 mL concentrated hydrochloric acid (HCl) in a desiccator for 7 hours. After acidification, samples are dried to remove excess HCl.

Due to the limited amount of sample powder for Box 15, residual acidified samples from TIC measurements were thoroughly rinsed with DI water, and dried. Isotope compositions were analyzed by combustion on an EAIsolink elemental analyzer coupled to a Delta V IRMS in continuous flow mode. Samples are corrected to standards USGS 40 (-26.39‰), Buffalo River Sediment (-19.86 ‰), and Bovine Liver (-17.78‰).

Precision based on replicate analysis of standard material is lower than 0.22‰.

Bulk Nitrogen Isotopes

Bulk N-isotope ratios are used in this study to determine nutrient availability in the marine environment. Care was taken to ensure nitrogen was not inadvertently removed during sample preparation. Some nitrogen studies include an acid rinse of

samples to remove inorganic carbon (e.g., Luo et al., 2016), however in organic geochemistry, acid rinsing, when followed by the removal of the supernatant, is routinely used to remove nitrogen compounds from samples (e.g., Niewenhuize et al., 1994). Therefore, the sediments were not acidified prior to N-isotope analysis. To measure N-isotopes, 60 mg of powder sample were weighed into tin capsules, combusted in an EAIsolink, and analyzed on a Delta V plus IRMS. Samples are corrected to standards USGS-40 (-4.52‰), IAEA N-1 (0.40‰), and Buffalo River Sediment (4.01‰). Precision based on replicate analysis of standard material is lower than 0.2‰.

Sulfur Isotopes and Sulfide Concentrations

Pyrite sulfur is extracted from sample powders by acid distillation in an inert atmosphere (Canfield et al., 1986). Approximately 0.5 g of sample was reacted in a nitrogen purged vessel with 1.0 M chromium chloride and 0.5 M HCl and boiled for ~2 hours to release sulfide from pyrite. The released hydrogen sulfide gas was then trapped in a 3% zinc acetate trap, in which sulfide gas was converted to zinc sulfide. A 3 mL split of zinc sulfide was taken to determine sulfide concentration colorimetrically (Cline, 1969) on a HACH spectrophotometer. These measured concentrations were used to calculate concentrations of pyrite in bulk rock sample assuming the stoichiometry of FeS₂. A 3% silver nitrate solution was added to the remaining trap solution to convert zinc sulfide to silver sulfide (Ag₂S). The sulfide was then filtered, dried, and homogenized. To measure S-isotopes, 0.2 mg of Ag₂S samples were weighed into tin capsules, combusted in an EAIsolink, and analyzed on a Delta V plus IRMS. Samples are corrected to standards IAEA S1 (-0.3‰), IAEA S2 (22.62‰), and IAEA S3 (-32.49‰). Precision based on replicate analysis of standard material is lower than 0.26‰.

Total Carbon (TC) and Total Inorganic Carbon (TIC)

TC measurements included the concentration of organic and inorganic carbon in the samples. TIC measurements will only include inorganic carbon from carbonates. TC and TIC concentrations were analyzed on an ELTRA Carbon-Sulfur Analyzer CS-580. Approximately 200 mg of sample powder are weighed into ceramic boats and combusted in a 1350°C furnace. TIC was measured by weighing 200 mg of sample powder and acidifying it with 50% phosphoric acid in the acidification module on the ELTRA. The amount of sample CO₂ evolved by combustion or acidification was detected by infrared absorption. The CO₂ yield from samples was calibrated using Buffalo River Sediment standard for TC (3.351% ± 0.017%) and AR4013 standard for TIC (2.81% ± 0.08). The total organic carbon (TOC) fraction was calculated as the difference between TC and TIC.

RESULTS

Total Inorganic Carbon (TIC) and Total Organic Carbon (TOC)

TIC values range between 0.01% and 11.86% and are inversely correlated with TOC (Figure 8). The higher TIC values occur within the limestone beds and these concentrations decrease within the shale lithology. TOC values have a much narrower range between 0% and 1.98%. Samples with higher TIC values correspond to those with little to no TOC. This is likely due to a dilution effect from higher amounts of CaCO_3 in limestone samples.

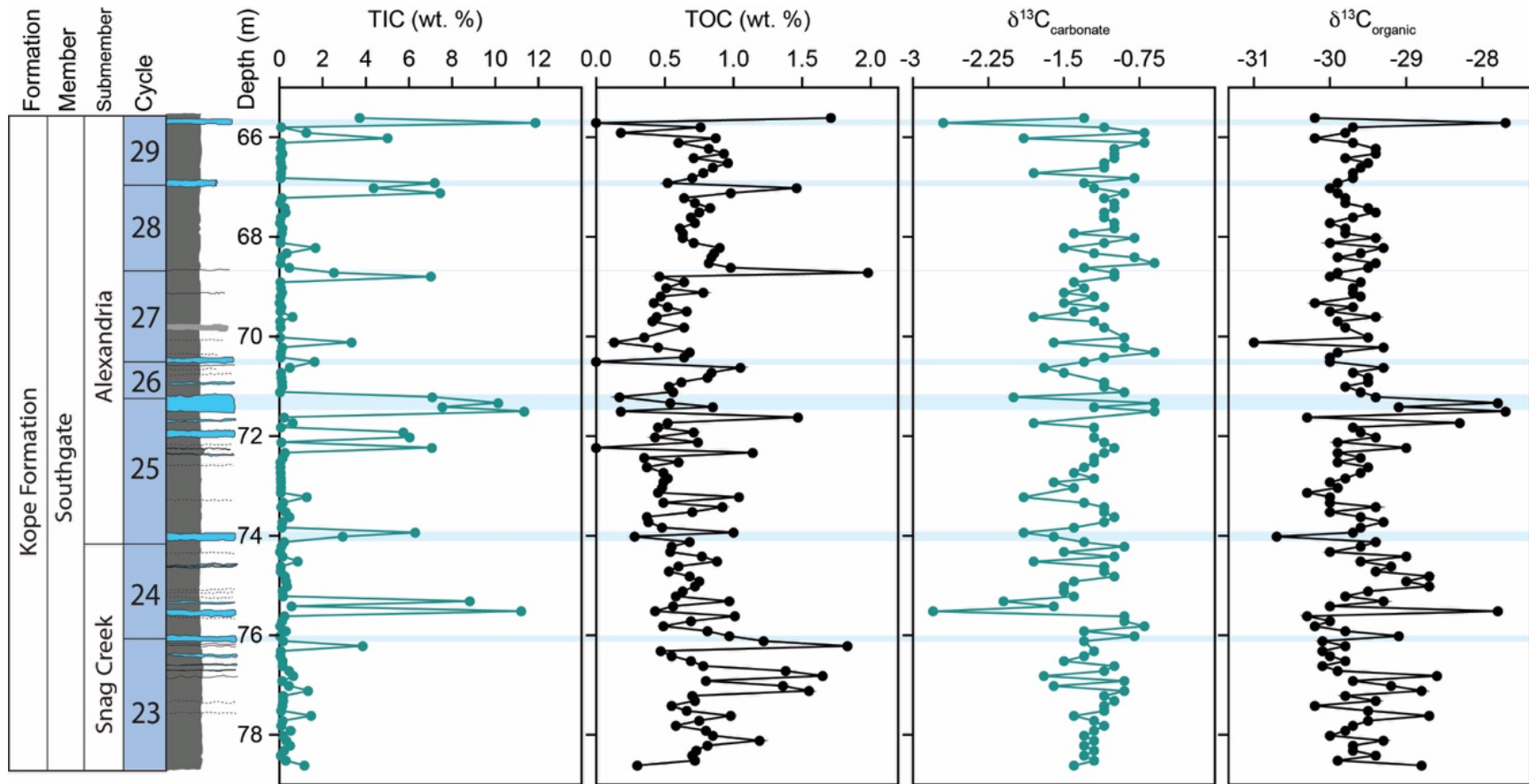


Figure 8. Downcore concentrations and C-isotope compositions total inorganic carbon and total organic carbon.

Organic Carbon Isotopes

The C-isotope values of organic matter ($\delta^{13}\text{C}_{\text{org}}$) show little variability throughout the core, ranging between -31.0 and -27.7‰ (Figures 8 and 9). The lowest values coincide with decreases in TOC (e.g., 70.12 m); however, higher $\delta^{13}\text{C}_{\text{org}}$ values do not necessarily coincide with higher concentrations of TOC (e.g., 71.74 m and 75.52 m). Overall, $\delta^{13}\text{C}_{\text{org}}$ values show a weak relationship with 10-meter scale cycles and do not exhibit cyclical variability.

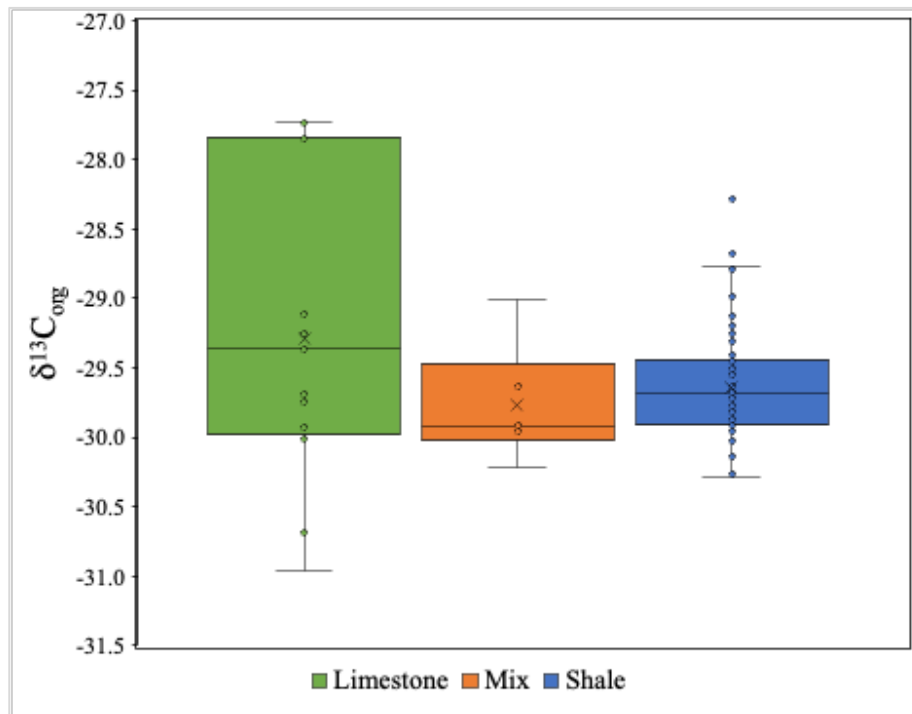


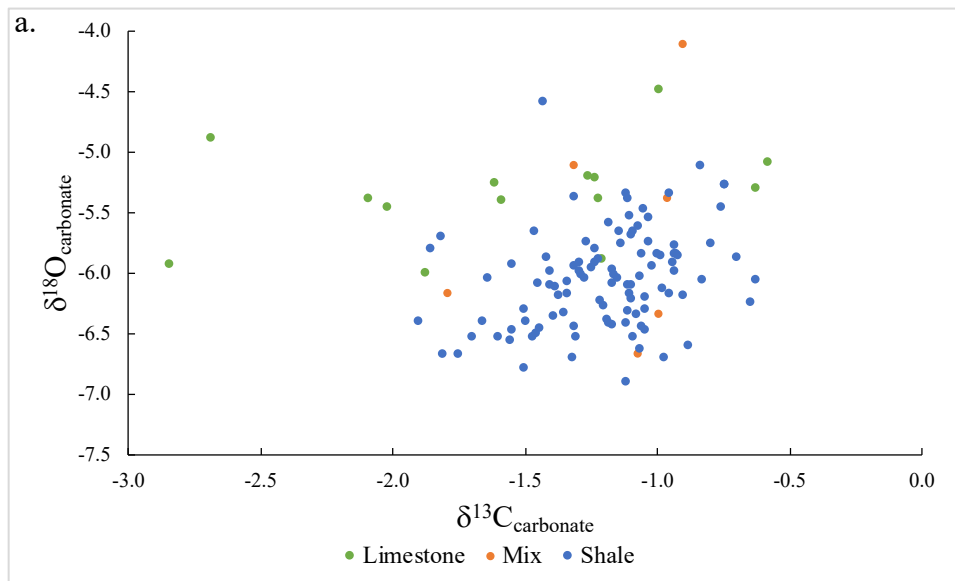
Figure 9. Boxplot of $\delta^{13}\text{C}_{\text{org}}$ data grouped by lithology. Limestone average is -29.3‰, n=15. Mix average is -29.8‰, n=6. Shale average is -29.6‰, n=109.

Inorganic Carbon and Oxygen Isotopes

C-isotopes of carbonates ($\delta^{13}\text{C}_{\text{carbonate}}$) show little variability, ranging between -2.8 and -0.6‰ (Figures 8 and 10b). Isotope values are invariant upsection through C23 but decrease to a minimum value of -2.8‰ in C24 at 75.52 m. Through C25, values increase to a maximum value of -0.6‰ at 71.34 m. From the bottom of C26 (~71 m) through the

bottom of C29 (~67 m) values are between -2.0 and -0.5‰ before decreasing to a minimum of -2.7‰ at 65.71 m at the top of the core.

O-isotopes of carbonates ($\delta^{18}\text{O}_{\text{carb}}$) also show a limited range in values between -6.9‰ to -4.1‰. From the bottom of the core through the top of C24 at 74 m isotope values do not show major increases or decreases. At the bottom of C25 there is a minimum value of -6.9‰ at 73.43 m. Values gradually increase to -5.1‰ at 71.51 m at the top of C25 and decrease once again through C26 and C26 until another minimum value of -6.7‰ is reached at 69.03 m. Values increase through C28 and C29 until an overall maximum value of -4.9‰ is reached at the top of the core at 65.71 m. A scatter plot of O- and C-isotope values shows no correlation, suggesting there is no significant meteoric water influence (Figure 10a).



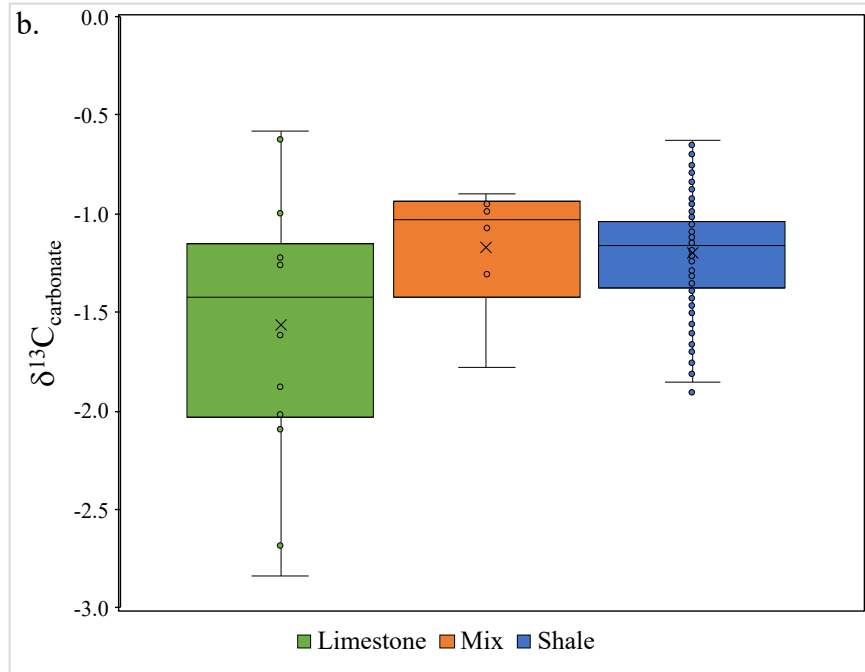


Figure 10. (a) Scatter plot of $\delta^{13}\text{C}_{\text{carbonate}}$ and $\delta^{18}\text{O}_{\text{carbonate}}$ by lithology showing no correlation. (b) Boxplot of $\delta^{13}\text{C}_{\text{carbonate}}$ data grouped by lithology. Limestone average is -1.6‰ , $n=14$. Mix average is -1.2‰ , $n=6$. Shale average is -1.2‰ , $n=106$.

Sulfur Isotopes

The S-isotope composition of pyrite ($\delta^{34}\text{S}_{\text{py}}$) extracts show an extraordinary range of 64.5‰ throughout the core (Figure 11). In addition, variability ranges greatly between samples. For example, between the two samples at 75.62 m and 75.52 m, S-isotope values show a 26.8‰ change. The variation exhibits a systematic cyclicality that appears to be concordant with meter-scale cycles and changes in lithology. S-isotope values are relatively low (-10.4‰) at lithological boundaries (e.g., at 74.02 m), increase to maximum values mid-boundary ($\sim 29\text{‰}$) and decreases to lower values ($\sim -15\text{‰}$) at the next cycle boundary. This pattern is most notable starting at cycle 23 up-section through cycle 26.

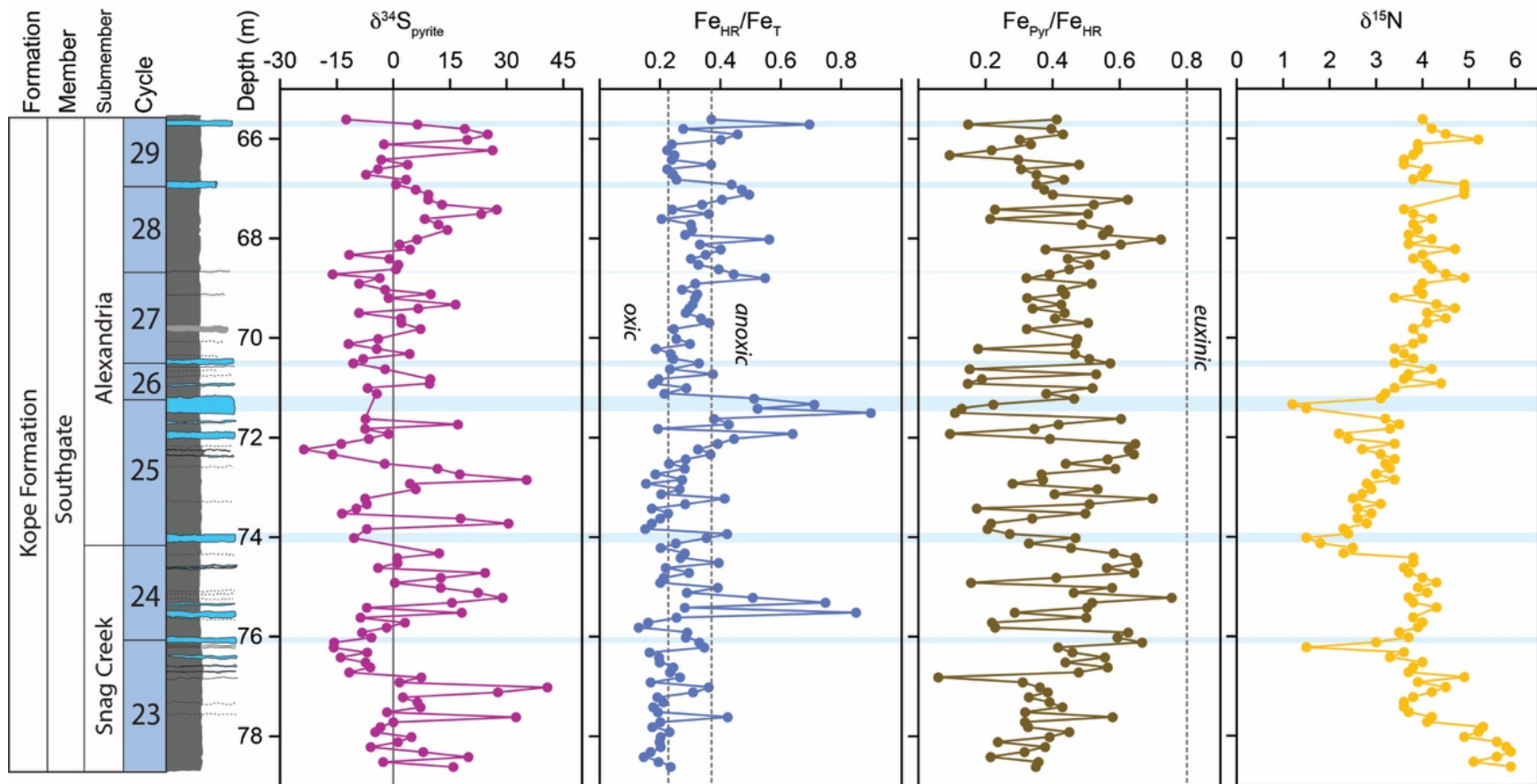


Figure 11. Downcore S-isotope composition of pyrite, reactive iron, and N-isotope composition of total nitrogen.

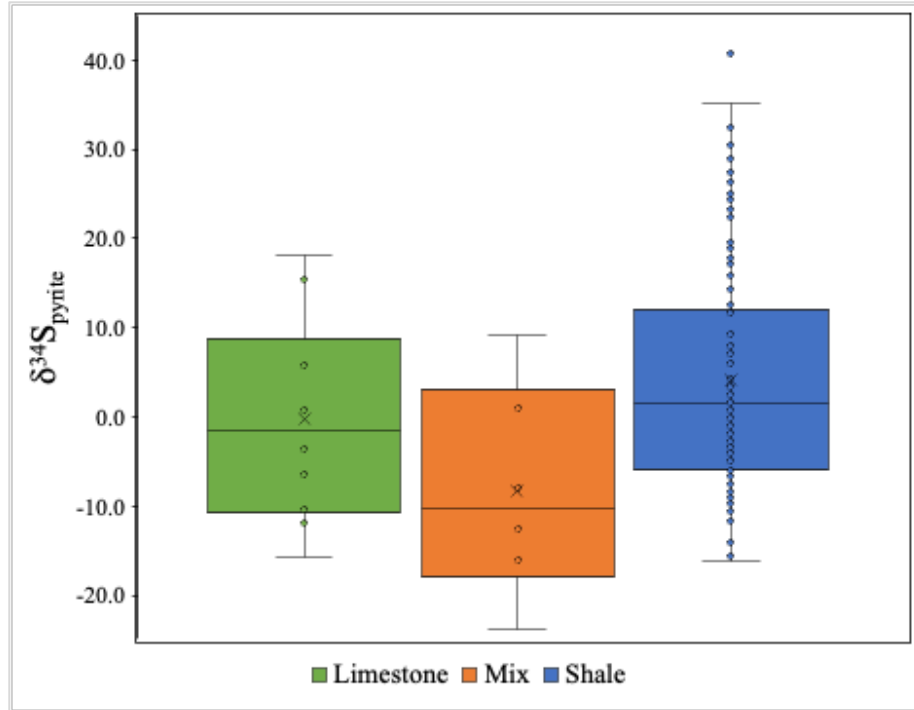


Figure 12. Boxplot of $\delta^{34}\text{S}_{\text{pynite}}$ grouped by lithology. Limestone average is -0.2‰ , $n=10$. Mix average is -8.3‰ , $n=6$. Shale average is 4.2‰ , $n=102$.

Reactive Iron

$\text{Fe}_{\text{HR}}/\text{Fe}_{\text{T}}$ ratios range between 0.13 and 0.90 throughout the core section, with two gradual shifts to maximum values (Figure 11). Through cycle 23 (78.62 m to 75.92 m), the ratios oscillate between what is considered oxic (< 0.22) and possibly oxic/anoxic ranges (0.22-0.38). Ratios reach an overall minimum value of 0.13 at 75.82 m before gradually shifting to values above the anoxic threshold of 0.38. Ratios reach a peak value of 0.85 at 75.52 m and decreases to a low value of 0.20 at 74.92 m. Ratios oscillate again between oxic, possibly oxic/anoxic, and lower-end anoxic (>0.38) values upsection through ~ 73 m before gradually increasing through cycle 25 to an overall maximum value of 0.90 at 71.51 m. From the bottom of cycle 26 (71.12 m) to the top of the core at 65.61 m, ratios oscillate once again between oxic, possibly oxic/anoxic, and low-end anoxic ranges.

Of 130 samples, 66 are within the possibly anoxic range, 35 within the oxic zone, and 28 in the anoxic zone. Of the anoxic samples, 25 fall within the ratio for ferruginous conditions ($Fe_{py}/Fe_{HR} < 0.7$) and 3 are above the ratio of euxinia ($Fe_{py}/Fe_{HR} > 0.7$).

Nitrogen

There is no significant relationship between TN and TOC (Figures 13a and 13b). The fraction of TOC of the total amount of carbon; however, shows a significant positive correlation with TN (adjusted r^2 is 0.4942, p-value is <0.05 ; Figure 13c). The same significant positive correlation is observed in shales (adjusted r^2 is 0.3374, p-value is <0.05), but is weaker in mixed lithologies (adjusted r^2 is 0.1736, p-value is >0.05), and absent in limestones (Figure 13d). The low sample count of mixed and limestone lithologies may account for the lack of significant relationships. A cross plot of Al and TN show a significant correlation in all samples (adjusted r^2 is 0.8414, p-value is <0.05 , Figure 13e) and each lithology (shale adjusted r^2 is 0.7489 and p-value <0.05 , mix adjusted r^2 is 0.9819 and p-value is <0.05 , limestone adjusted $r^2=0.7246$ and p-value is <0.05 , Figure 13f). In contrast, there is no relationship between $\delta^{15}N$ and TIC in the samples or lithologies (Figures 14a and 14b). There is a lack of correlation between $\delta^{15}N$ and C/N between all samples as well as the corresponding lithologies (Figures 14c and 14d). There is also a lack of correlation between Al and $\delta^{15}N$ in all samples and their corresponding lithologies (Figures 14e and 14f).

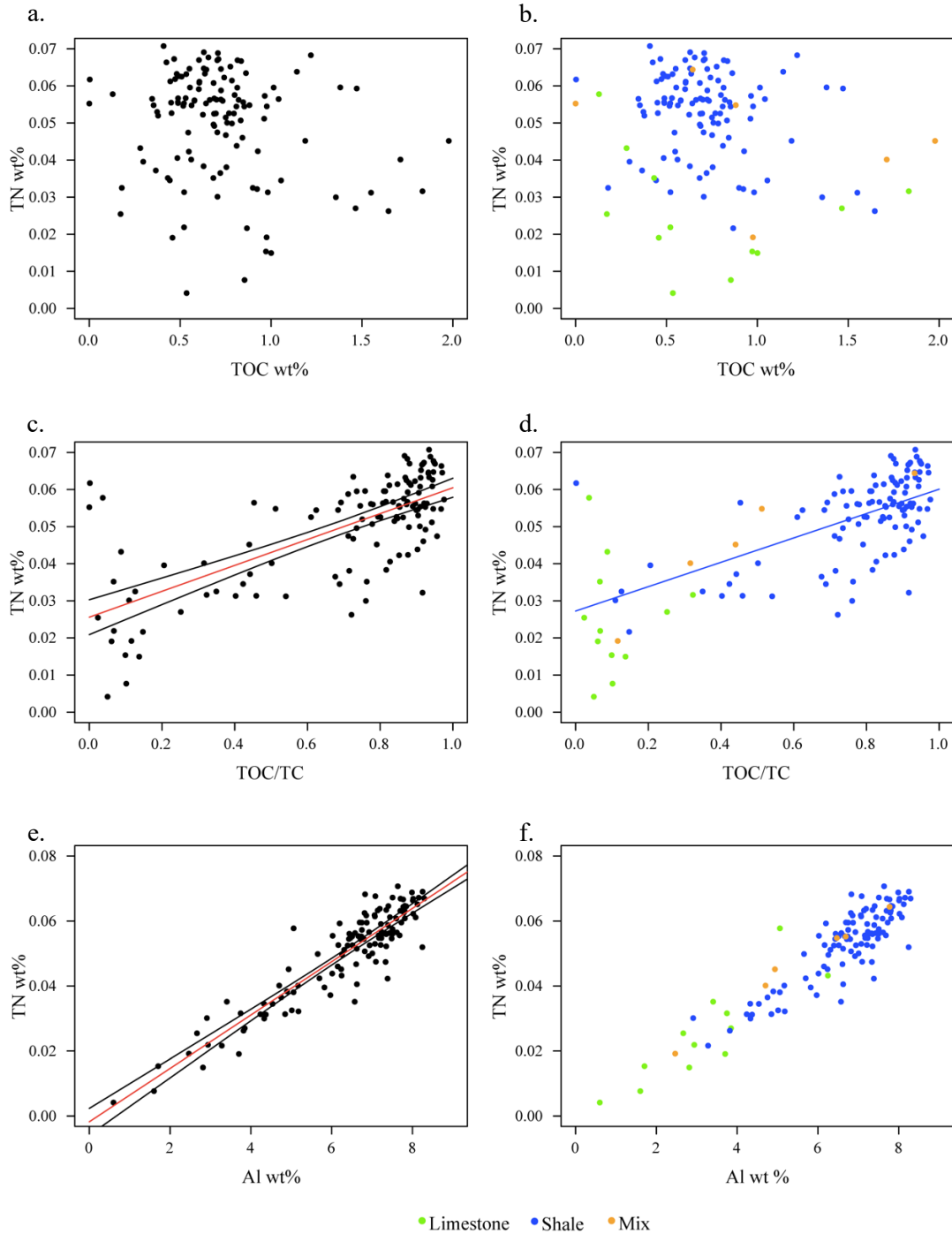


Figure 13. (a) Scatterplot of TOC and TN showing no correlation. (b) Scatterplot of TOC and TN with shale, mix, and limestone lithologies showing no correlation. (c) Scatter plot of TOC/TC and TN showing strong correlation. P-value is <0.05 and adjusted r^2 is 0.4942. (d) Scatter plot of TOC/TC and TN with shale, mix, and limestone lithologies. Shale P-value is <0.05 and adjusted r^2 is 0.3374. Mix and limestone lithologies do not show good correlation due to small sample size. (e) Scatter plot of Al and TN showing strong correlation. P-value is <0.05 and adjusted r^2 is 0.8414. (f) Scatter plot of Al and TN with shale, mix, and limestone lithologies. Shale P-value is <0.05 and adjusted r^2 is 0.7489. Mix P-value is <0.05 and adjusted r^2 is 0.9819. Limestone P-value is <0.05 and adjusted r^2 is 0.7246.

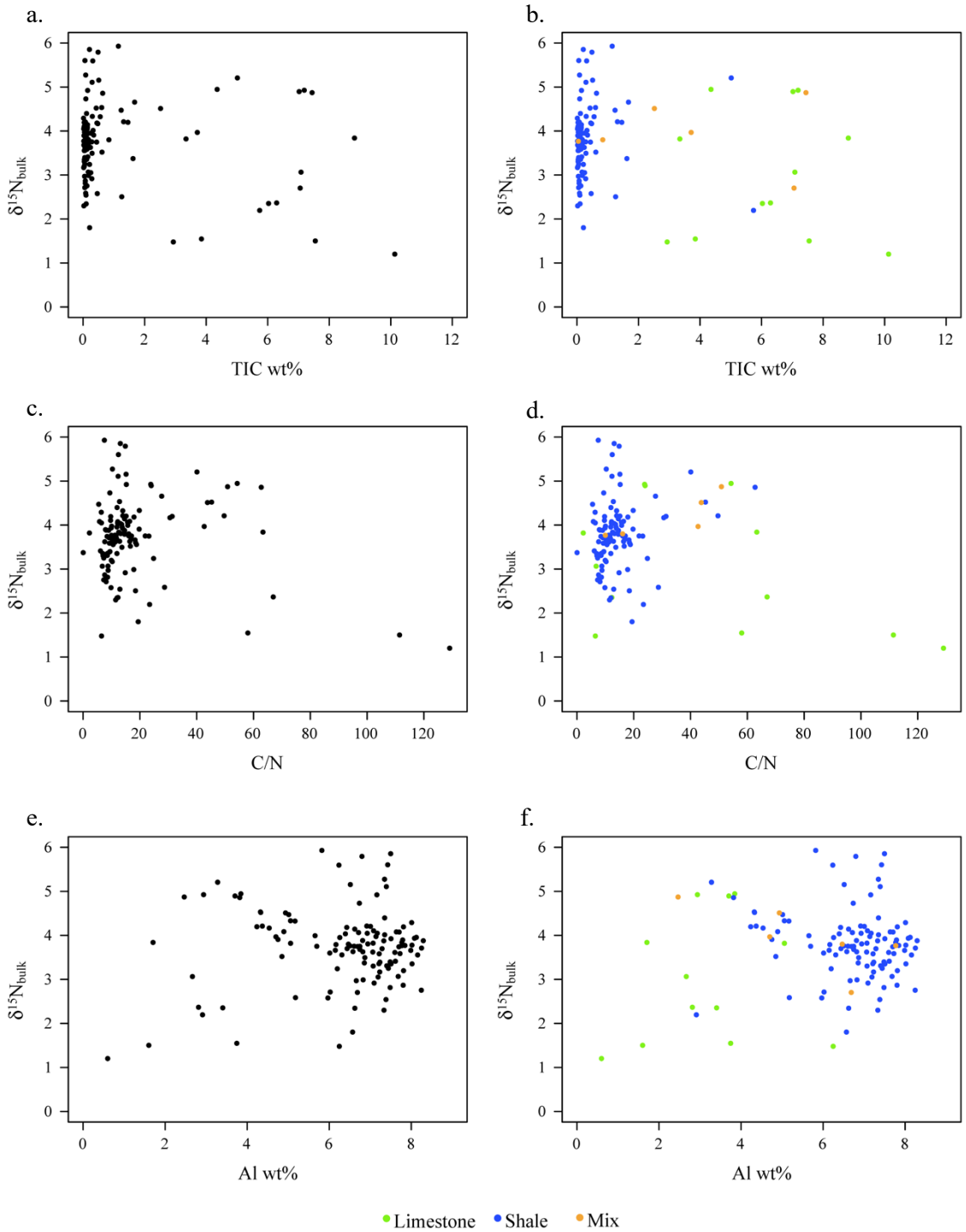


Figure 14. (a) Scatter plot of TIC and $\delta^{15}\text{N}$ showing no correlation. (b) Scatter plot of TIC and $\delta^{15}\text{N}$ with limestone, mix, and shale lithologies also show no correlation. (c) Scatter plot of C/N and $\delta^{15}\text{N}$ showing no correlation. (d) Scatter plot of C/N and $\delta^{15}\text{N}$ with limestone, mix, and shale lithologies also showing no correlation. (e) Scatter plot of Al and $\delta^{15}\text{N}$ do not show correlation. (f) Scatter plot of Al and $\delta^{15}\text{N}$ with limestone, mix, and shale lithologies also showing no correlation.

N-isotopes exhibit some variability with a total range of 4.7‰ (Figure 11).

Starting at the bottom of cycle 23 (78.62 m), values steadily decrease upsection from a maximum value of 5.9‰ to 1.5‰ at the bottom of cycle 24 (76.22 m). Values increase to a value of 4.3‰ within cycle 24 (74.92 m) and decrease to 1.5‰ at the boundary between cycles 24 and 25 (74.02 m). Isotope values increase steadily to 4.9‰ from cycle 25 through the top boundary of cycle 27 (68.80 m). The 3‰ increase in isotope value includes a minimum value of 1.2‰ at the boundary between cycle boundary 25 and 26 (71.34 m) and coincides with a lithology switch from shale to limestone. Through cycles 28 and 29 isotope values vary between 3.4‰ and 5.2‰. From cycles 23 to 26, decreases in N-isotope value coincide with lithology. This pattern is not as apparent in the top section of the core.

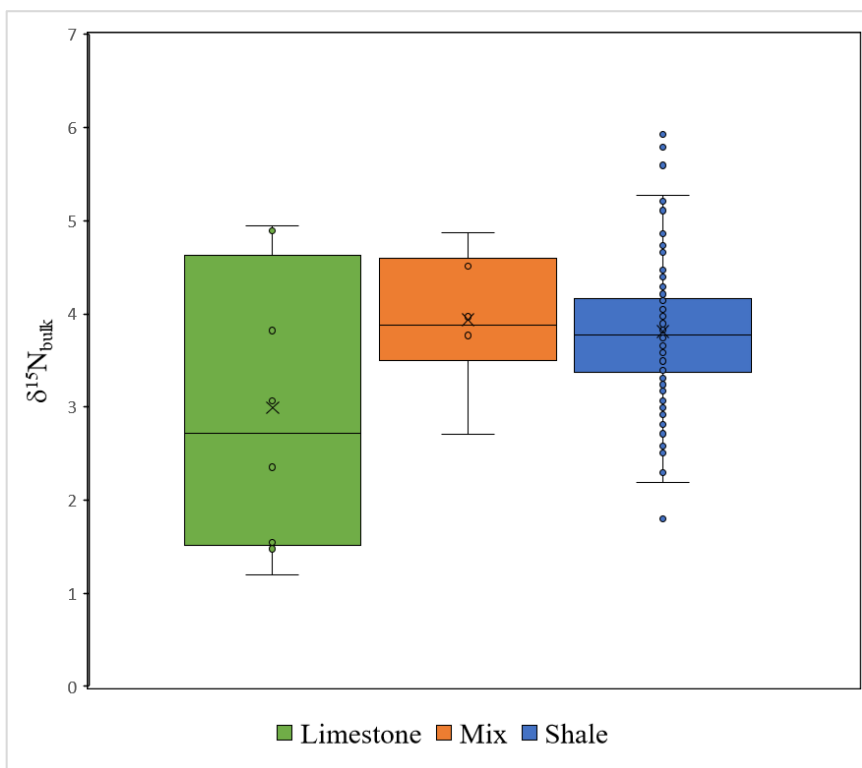


Figure 15. Boxplot of $\delta^{15}\text{N}_{\text{bulk}}$ grouped by lithology. Limestone average is 3.0‰, n=12. Mix average is 3.9‰, n=6. Shale average is 3.8‰, n=107.

DISCUSSION

The isotopes and elemental concentrations of sulfur, nitrogen, and carbon are used to understand past changes in Paleozoic environment and biogeochemistry; however, it is critical to determine whether the sediment archives that retain these chemical records were deposited in marine settings that were in open connection to the ancient ocean or in embayments of shallow epeiric seaways located further inland (Algeo et al., 2008). The broad shallow marine shelf of the Cincinnati located proximal to the uplift of the Taconic highlands (Figure 3) had complex hydrological conditions. Riverine input likely contributed to density stratification and delivery of dissolved solutes from continental weathering (e.g., Algeo et al., 2008). Stratification and ocean circulation patterns furthermore influenced redox gradients across the basin affecting the chemical inventory of seawater. Studies focusing on localized interactions of these integrated biogeochemical cycles are less numerous with many focusing on periods that exhibit major geochemical changes. With this, there is a lack of understanding in the extent in which localized changes can impact these global signals, especially in a period that lacked major perturbations in biogeochemical cycling such as the Kope formation.

The Kope formation was chosen for this study because it is not expected to show evidence for major changes in geochemistry. Since the late 1800's, the lithology and biostratigraphy of the Kope have been heavily studied and documented (e.g., Newberry, 1871; Meek, 1872). Fossil marker beds are now recognizable throughout the US and C-isotope studies for the Ordovician have aided in tracking different formations globally. Estimated to represent approximately 1.3 to 1.6 million years and deposited ~3 million years before the Hirnantian, the Kope formation lacks major global perturbations (e.g., C-

isotope excursion) in biogeochemical cycling (Ellwood et al. 2007; Kah et al. 2004). This makes it ideal for a high-resolution analysis of localized geochemical changes. The impact of these local effects, particularly changes in sedimentation driven by sea level fluctuations, can be seen in the sulfur, iron, and nitrogen signals of the Kope formation.

Carbon Cycling and Isotopes

Global and local changes in sea level affect the way carbon is cycled (Berner, 1991; Berner, 1994). CO₂ released into the atmosphere by volcanic outgassing is drawn down through carbon fixation by photosynthetic organisms. When these organisms die and sink to the sea floor, they are buried, and a small fraction of the organic remains are preserved as kerogen. The buried organic carbon is eventually released through tectonic activity and weathering. The carbon cycle can be very sensitive on short timescales especially during variable climate conditions like those of the Ordovician. Changes in the cycle can be recognized by positive C-isotope excursions which are abrupt increases in $\delta^{13}\text{C}$ on the order of 2-3‰ (Figure 5). Positive excursions occur when ¹²C becomes limiting by increased rates of primary productivity, which increases the amount of ¹³C retained in the rock record (Kump and Arthur, 1999). Alternatively, negative C-isotope excursions occur during a shutdown of the carbon cycle (Kump and Arthur, 1999).

Though productivity is typically interpreted to be the cause for C-isotope excursions, the drivers for these changes have been long debated. Previous studies suggest the pronounced C-isotope excursions were the result of global fluctuations in sea level. Finney et al. (1999) noted changes in lithology of Ordovician aged rocks in Nevada coincided with faunal changes and C-isotope excursions. From this they concluded C-isotope excursions are caused by sea level fluctuations. The idea was later refuted by

Bergstrom et al. (2010) who recognized that transgression and C-isotope excursions in the Cincinnati region and Estonia do not completely coincide. Thus, sea level fluctuations do not control global C-isotope excursions but may have effects on local geochemistry. Moreover, Holland et al (2001) revealed that the distribution of fossil assemblages in the Kope formation show subtle environmental controls on fossil distributions, such that biostratigraphic information is a better indicator of environmental changes, especially in the absence of obvious lithologic change.

It is important to note these studies use C-isotope records based on conodont and graptolite biostratigraphy, both are deep-water biofacies. Mudstone and limestones present in the Kope formation are indicative of shallow-marine facies, so those conodont and graptolite records may not necessarily reflect the biogeochemical variability occurring in the shallow environment of the Kope. Since the biostratigraphy and environmental turnover has been extensively studied in the Kope formation, it is an ideal location to study local and global constraints on chemostratigraphy as well as smaller scale nutrient cycles not previously recorded during climatic and environmental change that potentially occurred during the Late Ordovician.

In the Kope formation, the carbonate C-isotope values are generally invariant and fluctuate around -1.2‰ (Figure 8). This reiterates the idea that the Kope lacks global C-isotope excursions such as those typical in other parts of the Ordovician. While the positive C-isotope excursions in the Ordovician are accredited to carbon burial and changes in the global carbon cycle (Edwards and Saltzman, 2014), the invariant nature within the carbonate C-isotope values suggest the local dissolved inorganic carbon pool was relatively stable. When compared to the C-isotope plot of the Late Ordovician in the

Cincinnati region (Bergstrom et al., 2010), the C-isotope values for the Kope are lower. However, lack of an exact match is not surprising as the Bergstrom curve is based on data collected from conodonts, a deep-water marine organism, while the Kope is considered a shallow depositional environment. The sampling in this study is also at a much higher resolution than the data presented by Bergstrom et al (2010). While this carbonate signal does not reveal any major geochemical changes, the approximate match to the Bergstrom curve does confirm the stratigraphic location of this dataset within the Kope. In addition to chemostratigraphy, the carbonate isotopes in the Kope formation reveal vital information about post depositional alteration. Since the carbon and oxygen isotopes of carbonates lack covariance, it suggests no significant meteoric water influence, which agrees with interpretations based on petrography. Organic C-isotopes for the Kope formation are also invariant with only a $\sim 3\%$ range and TOC remains low throughout the core between 0-2 wt% (Figure 8). Both suggest there were no major changes in productivity or organic carbon burial.

Sulfur and Iron

While there is lack of significant geochemical changes in the isotopic signals of carbonate or organic carbon, these carbon signals may have a substantial impact on sulfur cycling. As C-isotope excursions are attributed to changes in the amount of carbon burial produced by primary productivity, the amount of organic matter burial will, in turn, affect the rate of microbial sulfate reduction and organic matter decomposition. In the Kope formation, rapid and systematic changes in S-isotope composition (Figure 11) suggest localized influences on biogeochemistry, rather than global changes in pyrite burial. The deposition time estimated for the Kope formation is approximately 1.3 to 1.6 million

years (Ellwood et al. 2007). When compared to the significantly longer residence time of 10^6 years for seawater sulfate (Kah et al., 2004), S-isotopic variation during pyrite burial occurs on million-year time-steps (Ellwood et al. 2007; Kah et al. 2004). This suggests that the rapid and constant fluctuation between high and low S-isotope values cannot be explained by variations in the global marine sulfur cycle. Pasquier et al. (2021) have made this observation in shelf and deep basin marine sediments over the past 40 Ma in the Eastern New Zealand Oceanic Sedimentary System. The S-isotope variability of pyrite in shelf sediments reflect sedimentary drivers that are on time scales much shorter than the residence time of sulfate in seawater. In comparison, deep basin pyrite S-isotope variations, however, reflect regional changes in bottom waters.

The sensitivity of S-isotopes to localized sulfur cycling has been observed in other modern marine sediments as well. Liu et al. (2019) suggested that pronounced changes in sedimentation rates greatly influence pyrite S-isotope values of Pleistocene aged sediments in the East China Sea inner shelf. They observed that the accumulation of thick layers of sediment during periods of high sedimentation rates controlled by the East Asian winter monsoon coastal currents, prevented the exchange of sulfate between porewaters and the overlying seawater, creating a “restricted” system. Sulfide produced by microbial sulfate reduction is thus enriched in ^{34}S , resulting in a low fractionation between residual sulfate and porewater sulfide. The pyrite that precipitated from this pool of dissolved sulfide retained $\delta^{34}\text{S}$ values that were close to or equivalent to seawater sulfate. Conversely, during periods of lower sedimentation rates, the lack of sediment accumulation creates an “open” system which allows better exchange of sulfate between porewaters and the overlying seawater. The sulfide produced by microbial sulfate

reduction in this case is depleted in ^{34}S and the inclusion of oxygen in the porewaters also promote reoxidation and disproportionation. This further depletes ^{34}S , produces a larger fractionation between sulfate and sulfide, resulting in pyrite with low $\delta^{34}\text{S}$ values (Pellerin et al., 2015).

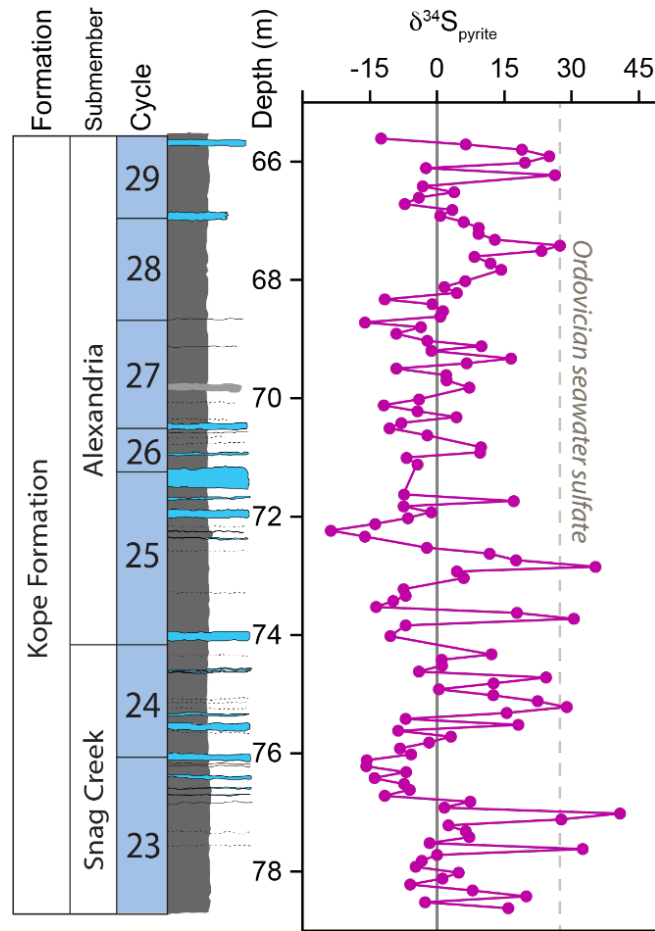


Figure 16. Downcore variation in the S-isotope composition of pyrite. The isotopic composition of Ordovician seawater sulfate (approximately 24‰; Kampschulte and Strauss, 2004) is indicated by the dashed line.

Like the East China Sea inner shelf, the Kope formation was highly affected by changes in sediment deposition. The pyrites with higher $\delta^{34}\text{S}$ values are generally located within the shale (cycles 23, 24, 25, 28, and 29; Figure 16). Sedimentologically, the shales correspond with episodes of rapid sedimentation (Figure 17) where higher $\delta^{34}\text{S}$ values, that approximate Ordovician seawater sulfate value of ~24‰ (Kampschulte and Strauss,

2004), are found towards the center of these deposits. In contrast, the sections with more limestone, associated with periods of lower sedimentation rates, have lower $\delta^{34}\text{S}$ values. The lower $\delta^{34}\text{S}_{\text{py}}$ values are associated with a change in lithology from shale to limestone, suggesting the isotope values of sulfur in pyrite are controlled by the same mechanisms that control lithology. Compared to the isotopic variability of these sequences, cycles 26 and 27 have more muted isotopic variability.

Although the Liu study focuses on marine sediments from a deep-water environment that are not directly comparable to the shallow carbonate ramp environment of the Kope, sea level fluctuations have also been tied to variance in $\delta^{34}\text{S}$ of pyrites. Pasquier et al. (2017) looked at the influence of sea level change during glacial and interglacial periods in marine sediments deposited over the last 500 ky in the northwestern Mediterranean basin. High $\delta^{34}\text{S}$ values are attributed to low sea levels during interglacial periods, while decreased and less variable $\delta^{34}\text{S}$ are attributed to high sea level during glacial periods. The direct connection between sea level change and $\delta^{34}\text{S}_{\text{py}}$ were explained by two possible, but not mutually exclusive, mechanisms: faster microbial sulfate reduction rates driven by changes in sedimentation or by changes in the connectivity of sediment porewaters where pyrite forms.

In a similar way to these studies, the Kope formation must be capturing strong localized effects. Sea level fluctuations either moved the seashore further inland, which decreased sediment input offshore, or seaward, which increased sediment input from the nearby Taconic Mountains. Strong storms potentially enhanced both scenarios by reworking and concentrating sediment-starved carbonate shell beds or greatly increasing sediment input, blanketing the seafloor with thick layers of sediment. Evidence for this is

seen in the abrupt switches in lithology and fluctuating $\delta^{34}\text{S}$ values. In this section of the Kope, the $\delta^{34}\text{S}$ of pyrite in limestones are on average lower than the $\delta^{34}\text{S}$ values of pyrite in shales and mixed sediment types (Figure 12). However, there is considerable overlap between the ranges of the three lithologies which makes it difficult to argue changes in lithology alone explain the variance in $\delta^{34}\text{S}$. In addition to the changes in sedimentation rate and sea level, S-isotopes in the Kope formation may be influenced by the cyclical migration of the sulfate reduction zone (SRZ).

While the change in sea level impacts the sedimentation rate, and lithology, it can also influence the location of the SRZ. Brett et al., (2008b) describe a model (Figure 17) that shows that during periods of sea level rise and sediment starvation, storm-related winnowing and reworking formed porous shell beds. These acted as conduits that allowed exchange of sulfate between seawater and the underlying sediments. The low sediment accumulation allowed for long periods of time with a stable SRZ and significant pyrite formation in the underlying shale beds. The S-isotope values of pyrite formed within the SRZ below this open exchange are more negative since sea water sulfate concentrations are not limited. As sea level fell and sedimentation rates increased, the newly accumulated sediment cut off seawater exchange and resulted in the upward migration of the SRZ. The S-isotope values of pyrite formed in the newly restricted porous shell beds and underlying sediments are mixed in value, reflecting a mix of early and later pyrite formation as the SRZ migrated upwards. S-isotope values of pyrite formed within thicker shales, or burial events, are mostly positive and close to the value of seawater sulfate (Figure 16), reflecting a closed and reducing environment with limited

sulfate concentrations. The SRZ continued to migrate to a new stable position during the following period of sea level rise, sediment starvation, and formation of a new shell bed.

This model is consistent with the oscillating pattern of S-isotope values in the Kope formation, (Figure 16). Within each cycle, values increase upsection to maximum $\delta^{34}\text{S}$ values close to the of Ordovician seawater sulfate, showing the migration of the SRZ during high sedimentation burial events located in shales. They then decrease to more negative values closer to limestone shell beds indicative of an open system. This pattern is apparent throughout the sections of the drill core sampled herein. Moreover, thin sections of the Kope formation show pyrite within shell and bryozoan fossils, and rip-up clasts within packstone. These are indicators of the different timings of pyrite formation and diagenetic histories recorded in a high-resolution section of rock. Thus, both timing and location of the SRZ account for the overlap in the range of $\delta^{34}\text{S}_{\text{py}}$ values of the three lithologies and overall sample-to-sample variance.

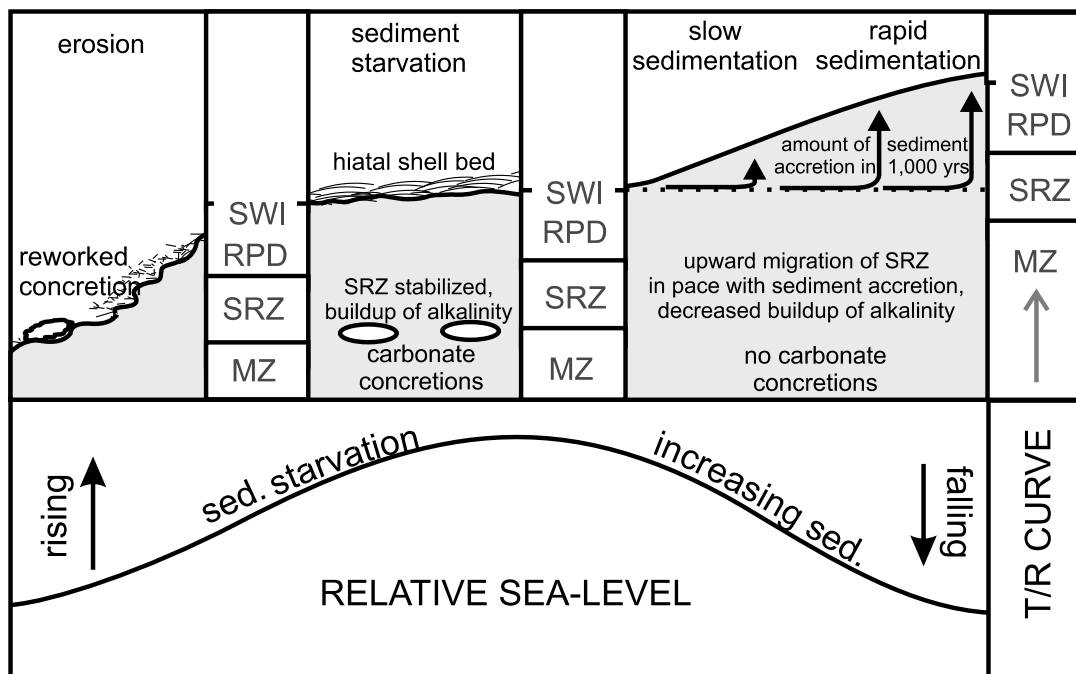


Figure 17. Relationship between sediment accumulation rates and sea level change. Bars show position of SRZ (sulfate-reduction zone), RPD (redox-potential discontinuity) and SWI (sediment–water interface) at different stages of a sea level cycle. From Brett et al., (2008b).

The distribution of reactive iron provides additional constraints on the timing and location (i.e., water column or porewaters) of pyrite formation, and therefore the paleoredox conditions. The reactive iron ratios are highly variable throughout the core (Figure 9). Most of the ratio data plot in areas that suggest possibly anoxic, ferruginous, or euxinic conditions (Figure 18); however, such an interpretation is inconsistent with the fossil record. The high diversity and abundance of benthic organisms in the Kope formation indicate that oxygen levels were sufficient to render the seafloor suitable for colonization (Brett et al., 2008b). This can be contrasted to the coeval deposits of the deep facies organic-rich Utica Shale, which has low biological diversity, and the fauna that are present are associated with low oxygen conditions (e.g., Baird and Brett, 2002). Therefore, suboxic to anoxic conditions are inconsistent with the paleobiology in the Kope.

It is also notable that the ratio values are related to lithology type. The shale data plot within the field for oxic to low oxygen conditions, the limestones are mainly within the ferruginous space, and mixed lithologies span anoxic to ferruginous regions of the cross-plot (Figure 18). The highest Fe_{HR}/Fe_T values are found in carbonates, but this is unsurprising since this lithology has lower amounts of unreactive iron (siliciclastic iron). This dilution of siliciclastic iron pushes Fe_{HR}/Fe_T toward higher values that would artificially indicate anoxic conditions. Furthermore, the migration of the SRZ during sea level fluctuations may recycle iron through reductive dissolution, which can also artificially enrich reactive iron concentrations. Similar patterns of iron redistribution were observed by Farrel et al., (2013) where Fe_{HR} in Late Ordovician-aged trilobite beds suggested anoxic water column conditions despite the nearly continuous presence of fossilized in situ benthic fauna. Fe_{HR}/Fe_T is interpreted as a water column signal, but the water column signal itself can be altered by episodic sedimentation and recycling of iron (Coleman, 1985; Farrel et al., 2013). Therefore, it is important to consider depositional context when using the reactive iron proxy. The mismatch between iron ratios and fossil evidence for oxygen availability and the correspondence with lithology within the Kope suggests alternative interpretations of the reactive iron speciation are needed.

Total iron and unreactive iron are highest in shales, which is consistent with the higher amounts of siliciclastic input during their deposition (Figure 19). Of the reactive iron fractions, carbonate and pyrite iron are the most abundant. When normalized to Al, there is clear grouping between values, their corresponding lithology, and the amount of Al in the system. When normalizing the total amount of iron to aluminum, most samples

have ratio values greater than 0.66, indicative of iron enrichment. The Fe_T/Al are used as a proxy to determine if there is authigenic iron enrichment relative to the total iron pool in sediments and is generally-used as a signal of anoxic environments (Raiswell et al., 2018). Though the threshold value is derived from oxic sediments, these interpretations still require geological context. Like the Fe_{HR}/Fe_T values, there is a dilution effect during periods of low siliciclastic, or Al, input that increases the Fe_T/Al ratio towards anoxic values. Limestone samples plot above the threshold since the total iron is driven by iron carbonate. Shale samples may plot above the threshold due to high amounts of pyrite, which may be early or later formed pyrite. As with sulfur, we see strong diagenetic effects with iron that are not necessarily indicative of water column redox. Instead, they are syndepositional and postdepositional alterations that are likely tied to sea level change, sediment delivery, and migration of the SRZ.

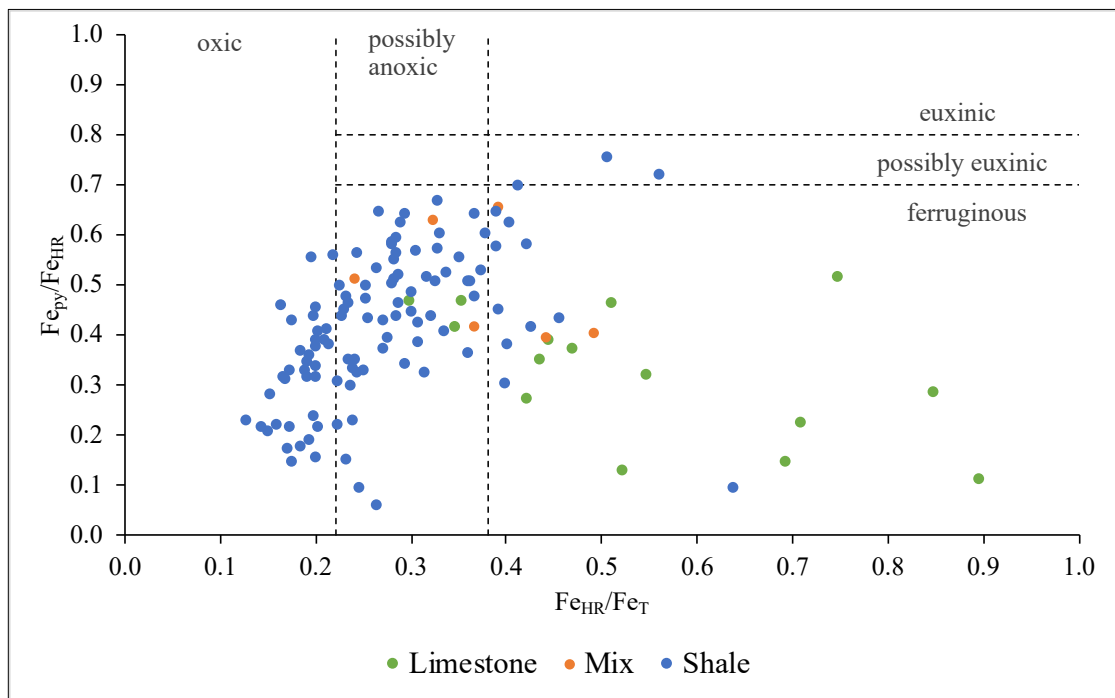


Figure 18. Scatter plot of Fe_{HR}/Fe_T and Fe_{Py}/Fe_{HR} showing the distribution of redox conditions of samples based on lithology.

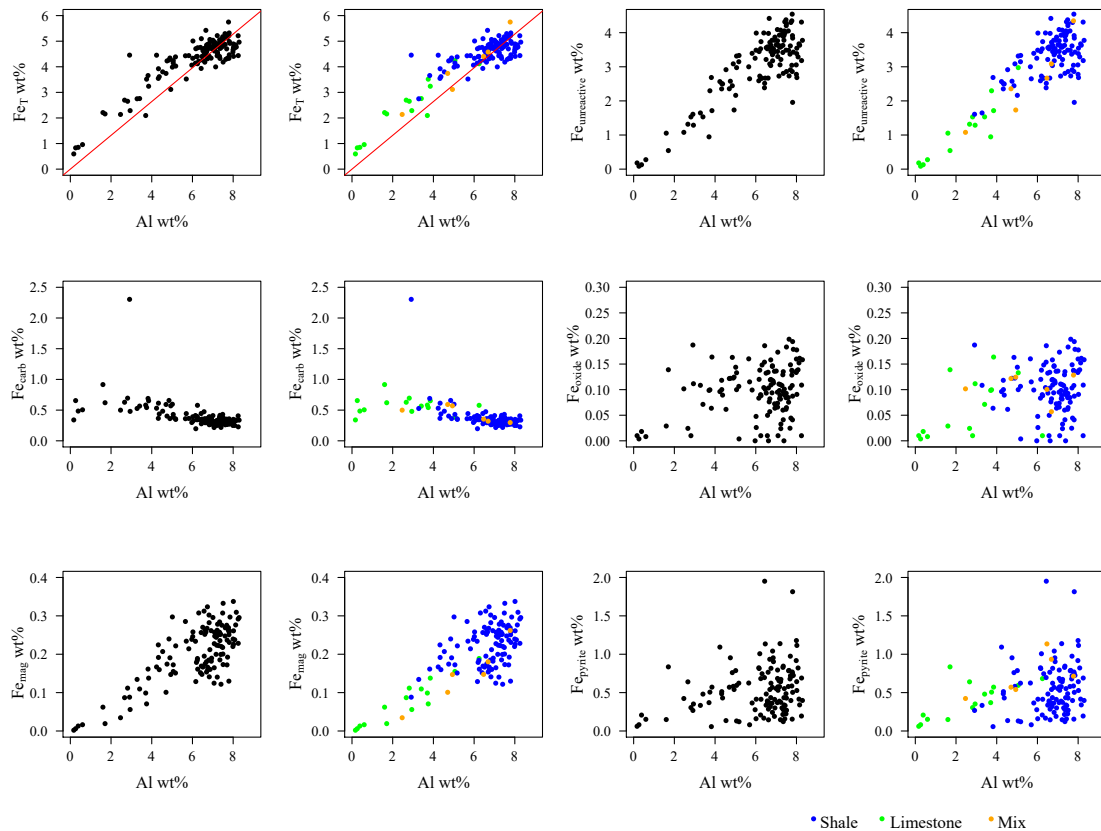


Figure 19. Cross plots of aluminum and each reactive iron species and the corresponding sample lithologies. Al vs Fe_T plots show a line with a slope of 0.66 which denote the threshold at which samples are considered to have authigenic iron enrichment.

Nitrogen Cycling and Isotopes in Marine Environments

In marine environments, nitrogen is an important bio-limited nutrient necessary for all life. Though abundant in the atmosphere today (~78%), nitrogen is limited in the ocean since it requires fixing to become bioavailable. Once bio-available, marine organisms primarily use nitrogen for structural components (e.g., nucleotides and amino acids) and as an energy source (Gruber, 2008). The marine nitrogen cycle (Figure 20) describes the several chemical transformations and five oxidation states nitrogen undergoes throughout this process. Though complex, the nitrogen cycle is useful for understanding nutrient availability in both present day and in the past. On geologic

timescales the most important nitrogen transformations are nitrogen fixation (N-fixation), denitrification, and nitrification. These are the main reactions which add and remove bioavailable nitrogen in the ocean. The balance of these reactions determines the size of the bioavailable nitrogen reservoir, which in turn will influence the amount of nutrients available for primary productivity.

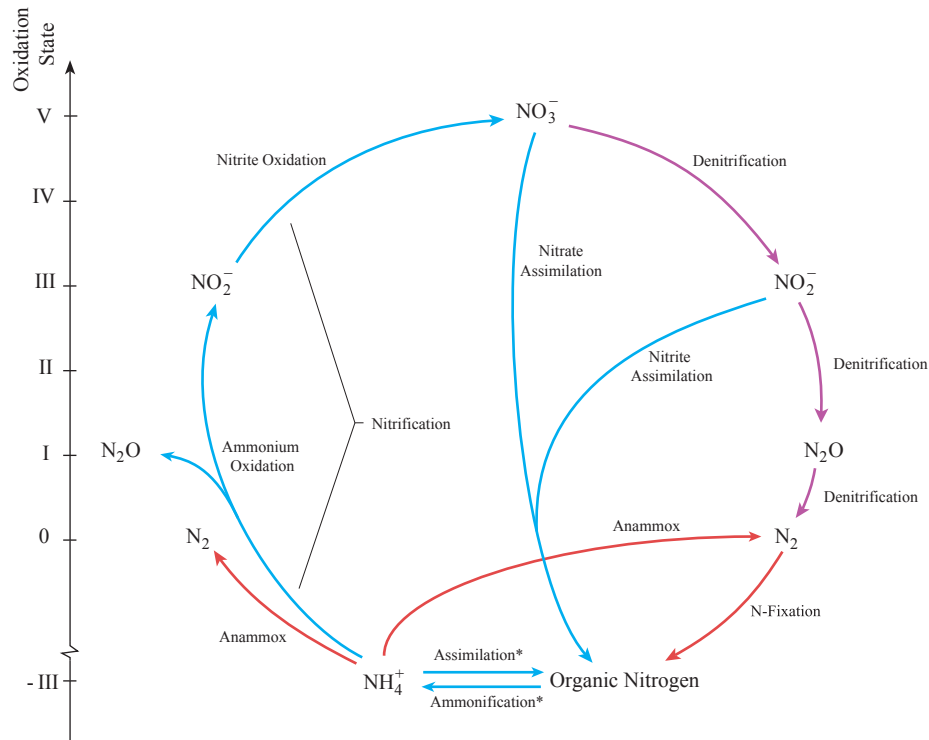


Figure 20. Major chemical forms and transformations of nitrogen in the marine environment and their oxidation states. The color of the arrows denotes the redox condition: blue = oxic, purple = suboxic, and red = anoxic. *Assimilation and Ammonification can occur in both oxic and anoxic environments. Modified from Gruber, (2008).

Changes in the balance of reactions and size of the nitrogen reservoir can be identified using N-isotopes. N-isotopes can be used as indicators of metabolic processes in primary producers to track nutrient cycling and redox conditions in aquatic environments. Organic matter particulates in the water column will have an N-isotope signature that reflects the composition of nitrogen assimilated by primary producers (Ader et al., 2016). These particulates are then buried and recorded in the sediment record

which can then be used to interpret the environmental conditions in which they formed. The major reactions in the nitrogen cycle, denitrification, nitrification, and N-fixation, are microbially mediated and have distinct N-isotope fractionations that occur at different redox states.

Denitrification is the sequential reduction of nitrate to nitrite, nitric oxide, nitrous oxide, and nitrogen gas (Table 1). During denitrification, bacteria utilize nitrate as an electron acceptor. These reactions are facilitated by the enzymes nitrate reductase, nitrite reductase, nitric oxide reductase, and nitrous oxide reductase (Gruber, 2008). It is important to note that from a biogeochemical perspective any process that results in the loss of nitrogen from the biosphere is referred to as a denitrifying process, including anammox (Devol, 2008). Denitrification is most prominent in suboxic (low-oxygen) conditions since the enzymes needed to convert nitrate to nitrogen gas are inhibited in the presence of high oxygen concentrations (Gruber, 2008). Relative to N-fixation and nitrification, denitrification has a large fractionation factor (up to 40‰) associated with its reaction and produces a high bulk sediment N-isotope value relative to N-fixation and nitrification (Delwiche and Steyn, 1970; Quan et al., 2013; Talbot, 2001; Wada, 1980). This occurs because as the lighter N-isotope is preferentially released as N-gas, the heavy N-isotope is incorporated into organic matter and buried (Quan and Falkowski, 2009). During denitrification, it is possible for nitrous oxide to escape into the atmosphere. Nitrous oxide has a global warming potential 265-298 times that of CO₂ and can have dramatic effects on climate when released in large quantities (IPCC, 2014).

Oxic	Suboxic	Anoxic
Nitrification $\text{NH}_4^+ \rightarrow \text{NO}_3^-$	Denitrification $\text{NO}_3^- \rightarrow \text{N}_{2(\text{gas})}$	Nitrogen- Fixation $\text{N}_2 \rightarrow \text{NH}_4^+$
Inhibited by light Requires O_2	Too much O_2 inhibits enzymes	O_2 inhibits reaction
Small $\delta^{15}\text{N}$ fractionation	Large $\delta^{15}\text{N}$ fractionation	Small $\delta^{15}\text{N}$ fractionation

Table 1. Dominant species of nitrogen in different redox conditions, their inhibitions, and relative isotope fractionations.

Nitrification is the conversion of ammonium to nitrate through a two-step reaction: oxidation of ammonium to nitrite and oxidation of nitrite to nitrate. This is most commonly driven by the ammonium oxidizer *Nitrosomonas* spp and nitrite oxidizer *Nitrobacter* spp. Nitrification requires the presence of oxygen and can be inhibited by light (Gruber, 2008). It produces a small fractionation (Up to 20 ‰), resulting in low bulk N-isotope values relative to denitrification (Delwiche and Steyn, 1970; Quan et al., 2013; Talbot, 2001; Wada, 1980).

Lastly, N-fixation occurs when nitrogen gas drawn from the atmosphere is converted into organic nitrogen. Nitrogen is usually fixed by photoautotrophic organisms but may also be fixed by other organisms such as unicellular bacteria and some cyanobacteria (Gruber, 2008). N-fixation is facilitated by the enzyme Nitrogenase; however, it must be done so in the absence of oxygen or the reaction is inhibited (Berman-Frank et al., 2007; Quan and Falkowski, 2009). Thus N-fixation can only occur in anoxic conditions. N-fixation produces a negative fractionation (as low as -6 ‰) which results in low bulk N-isotope values relative to denitrification (Delwiche and Steyn, 1970; Quan et al., 2013; Talbot, 2001; Wada, 1980).

Since each compound of nitrogen is associated with certain oxygen concentrations and isotope fractionations, N-isotope values of sedimentary organic matter can potentially be utilized to determine the redox conditions of the sediment and bottom water. Quan et al. (2013) constructed a conceptual model of the relationship between bulk N-isotope values and oxygen concentrations (Figure 21). In this model, the transition to increased N-isotope values may be indicative of suboxic conditions and the predominance of denitrification (Figure 21), steps 1 and 4. During denitrification, ^{14}N in nitrate is preferentially converted into N-gas leaving residual nitrate enriched in ^{15}N . The residual ^{15}N enriched nitrate is then incorporated into organic matter and buried. A shift towards lower N-isotope values suggest either an anoxic or fully oxic environment (Figure 21), steps 2 and 3. The different species indicate whether nitrogen was being added or removed from an ecosystem, which can be used to understand nitrogen cycling during the Ordovician. Though N-isotopes appear to be a promising method to determine these cycles, N-isotope information alone is not sufficient to determine whether nitrification or N-fixation were the predominant process of a given age or depth since both have relatively low isotope values. Additional redox proxies, such as reactive iron or trace metal analysis, are needed to differentiate between the two species and reconstruct the environment.

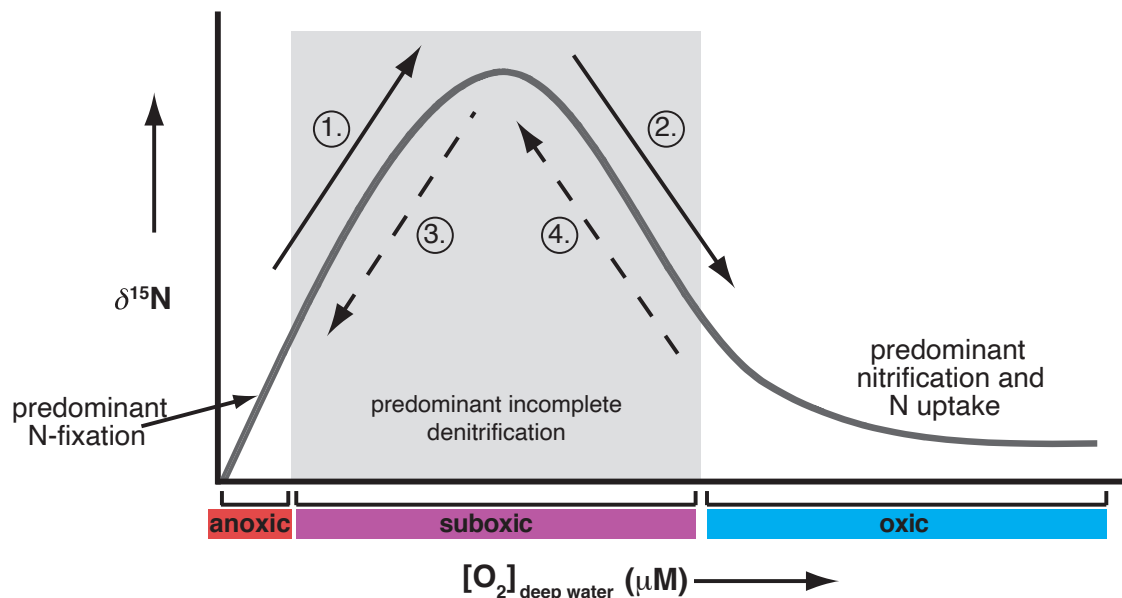


Figure 21. Relationship between oxygen concentrations and N-isotope values and their associated species of nitrogen in the nitrogen cycle. Modified from Quan et al., (2013).

Post-depositional processes may also affect isotope values and should be considered when measuring and interpreting N-isotope data. Nitrogen loss can occur during the metamorphic conversion of kerogen to graphite (Ader et al., 2016). This can be identified by a dramatic increase in the C/N values (Boudou et al., 2008; Daniels & Altaner, 1990; Volkova & Bogdanova, 1989).

Furthermore, NH_4^+ can substitute for K^+ in clay minerals during diagenesis due to their similar ionic radii which can alter the N-isotope value of the bulk sample, (Lehman et al., 2002; Robinson, 2012; Williams et al., 1995). NH_4^+ can be sourced from organic nitrogen that has been degraded in situ, or inorganic nitrogen from NH_4^+ in detrital clay minerals that is brought in through rapid sedimentation. In the absence of oxygen, NH_4^+ can replace K^+ in clays, but will have no fractionation effect and thus alter the N-isotope value by less than 1‰ from the primary signal (Ader et al., 2016; Fraga-Ferreira et al., 2021; Lehman et al., 2002). In an oxic environment NH_4^+ can oxidize to NO_2^- , NO_3^- , or

N₂, which can alter the primary N-isotope signal by up to 4‰ due to a fractionation effect during these reactions.

One method to evaluate if inorganic nitrogen has been incorporated into clay is to compare the total amounts of organic carbon and nitrogen in the sample. A positive correlation between total organic carbon (TOC) and total bulk nitrogen (TN_{bulk}) that goes through the origin can demonstrate that the nitrogen in the sample is associated with organic matter and therefore suggests the bulk N-isotope values are from organic nitrogen (Schubert and Calvert, 2001; Luo et al., 2016). A positive y-intercept would indicate there is more nitrogen than expected for TOC and likely comes from ammonium retained in siliciclastics. In addition, a lack of correlation between C/N_{bulk} and N-isotope value indicate there was no preferential uptake of nitrogen bound in ammonium during diagenesis (e.g., Luo et al., 2016; Schubert and Calvert, 2001).

The initial comparison between TN and TOC shows no significant relationship (Figure 13a). However, when compared to previous studies that have TOC values of up to ~12% (e.g., Luo et al., 2016), the apparent lack of correlation in this data set is likely due to the very low amounts of organic carbon in the samples (maximum value of ~2%) which creates a dilution effect from other material in the samples. Normalizing the amount of organic carbon to the total amount of carbon in the samples removes this effect to better represent these samples. The resulting plot shows a significant positive correlation (Figure 13b) and is consistent in all samples regardless of lithology (Figure 13c). A lack of correlation between $\delta^{15}\text{N}_{\text{bulk}}$ and TIC or C/N suggests there is no preferential value for $\delta^{15}\text{N}_{\text{bulk}}$ at any amount of inorganic carbon (up to 12%) or organic matter (Figures 14a-14d). The positive correlation and a y-intercept that is close to zero

between TN and TOC/TC indicate N-isotopes mainly reflect that of organic nitrogen. There is also a lack of correlation between Al and N-isotopes, suggesting the amount of Al does not influence the N-isotope value (Figures 14e-14f).

When interpreted in the context of the nitrogen and oxygen relationship described by Quan et al. (2013), it could be argued that as values decrease from the bottom of the core moving upsection there is a shift to anoxic conditions between the Snag Creek and Alexandria submembers. The anoxic conditions then led to increased denitrification, a buildup of the nitrogen pool, which in turn lead to an increase of N-isotope values from 2‰ to 5‰ at the top of the core section. However, this interpretation is difficult to support since the fossil beds are inconsistent with suboxic conditions, which implies that the positive N-isotope values are not indicative of denitrification in suboxic conditions. The presence of brachiopod, crinoid, and trilobite fossils as well as evidence of bioturbation throughout the core, and to a larger extent the Kope formation, are more consistent with oxic conditions that sustained benthic fauna on the seafloor. Akin to the S-isotope data, the N-isotope data may be capturing localized diagenetic effects.

N-isotope data show a dependency on lithology that support this interpretation. N-isotope values have a lower average in limestones than shale and mix lithology samples (Figure 15) and show pronounced decreases at limestone boundaries. When looking at reactive iron, Fe_{HR}/Fe_T increases appear to coincide with N-isotope decreases (Figure 11). Again, reactive iron data suggest anoxic conditions, but it is difficult to argue since limestones are primarily fossilized beds. Depositional context is important to note when using the iron proxy and the same can be argued for N-isotopes in the Kope formation. It is likely the N-isotope data show diagenetic reactions occurring below an oxic water

column. Lithology shows a strong influence associated with sea level turning on and off detrital input and some influence on nitrogen retention and delivery associated with clay availability.

CONCLUSION

The Kope formation data offer valuable input on the effects of diagenetic reactions on geochemical signals retained in the rock record. Though data interpretations in recent studies, such as those that argue for periods of widespread euxinia in the water column leading into the Hirnantian, are promising they may not fully account for diagenetic signals that can alter the primary signal. There can be ongoing processes leading into major geological events, so the interpretations of one geochemical proxy does not definitively mean it was the only event leading to the loss in biodiversity millions later in the Hirnantian. Moreover, the re-evaluation of fossil assemblages in the Paleozoic suggests the beginning of biological decline occurred much earlier in the Katian.

S-isotope data in the Kope formation show an extraordinary range of up to 64.5‰ throughout the core with large sample to sample variability. The isotope signal being captured in these samples represent a mix of pyrite formed at the time of deposition and during diagenesis. As sea level fluctuated, the amount of sediment delivery influenced the connection of sediment porewaters to overlying seawater sulfate and the location of the SRZ. This altered the primary signal recorded at the time of deposition. This is evident through higher S-isotope values, closer to Ordovician seawater sulfate values of ~24‰, within the center of shales where there was little to no exchange between the porewaters, and seawater and decreased to negative values near and at limestone boundaries where there was open exchange.

The reactive iron redox proxy suggests the water column was often a low oxygen environment, however the fossil assemblages found throughout the core suggest

otherwise. It is known that changes in sedimentation can mask the water column signal and create a dilution of siliciclastic iron. Moreover, the migration of the SRZ during sea level fluctuations may recycle iron through reductive dissolution, which can also artificially enrich reactive iron concentrations. Therefore, it is important to consider the depositional context when using the reactive iron proxy. For these samples, this proxy is not indicative of water column redox but instead captures an aggregate signal influenced by sea level, sediment delivery, and location of the SRZ.

Moving upsection, N-isotope data show an overall systematic decrease of 4.4‰, followed by a gradual increase of 3.4‰ which, when using the N-proxy alone, can be interpreted as a switch to increased denitrification in a low-oxygen setting. However, this interpretation is not consistent with the high diversity of fossils found in the Kope which require oxic environments. Instead, the N-isotope data capture the localized diagenetic reactions that occur below an oxic water column.

APPENDICES

Appendix A

Depth (m)	Lithology	TC wt %	TIC wt %	TOC wt %	$\delta^{13}C_{org}$	$\delta^{13}C_{carb}$	$\delta^{18}O_{carb}$	Pyrite S wt%	Pyrite wt%	$\delta^{34}S_{pyrite}$	$\delta^{15}N_{bulk}$	TN wt %	C/N
65.61	Mix	5.42	3.71	1.71	-30.2	-1.3	-5.1	0.66	1.31	-12.5	4.0	0.040	42.65
65.71	Limestone	11.54	11.86	0.00	-27.7	-2.7	-4.9	0.07	0.14	6.4	-		
65.80	Shale	0.83	0.08	0.76	-29.7	-1.1	-5.5	0.63	1.27	18.9	4.2	0.050	15.14
65.91	Shale	1.42	1.24	0.18	-29.8	-0.7	-5.3	0.90	1.81	25.0	4.5	0.033	5.50
66.02	Shale	5.88	5.01	0.87	-30.2	-1.9	-5.8	0.38	0.77	19.6	5.2	0.022	40.09
66.11	Shale	0.68	0.08	0.60	-29.7	-0.7	-5.3	0.46	0.91	-2.5	3.9	0.067	9.01
66.23	Shale	0.88	0.06	0.82	-29.4	-1.0	-5.3	0.25	0.49	26.3	3.9	0.056	14.61
66.33	Shale	1.06	0.13	0.93	-29.4	-1.0	-5.5	0.09	0.19		3.8	0.042	21.88
66.42	Shale	0.75	0.04	0.71	-29.8	-1.0	-5.7	0.39	0.78	-3.2	3.6	0.067	10.58
66.52	Shale	1.02	0.06	0.96	-29.5	-1.1	-5.7	0.86	1.71	3.8	3.6	0.051	18.81
66.61	Shale	0.95	0.10	0.85	-29.6	-1.1	-5.6	0.37	0.73	-4.1	4.1	0.054	15.67
66.72	Shale	0.85	0.07	0.78	-29.7	-1.8	-5.7	0.48	0.95	-7.2	4.0	0.065	11.90
66.82	Shale	0.77	0.06	0.70	-29.7	-0.8	-5.4	0.61	1.21	3.4	3.8	0.067	
66.92	Limestone	7.71	7.19	0.52	-29.9	-1.3	-5.2	0.40	0.81	0.7	4.9	0.022	23.82
67.02	Limestone	5.82	4.36	1.46	-30.0	-1.2	-5.4	0.66	1.31	5.9	4.9	0.027	54.27
67.12	Mix	8.42	7.44	0.98	-29.9	-0.9	-4.1	0.49	0.97	9.3	4.9	0.019	50.88
67.22	Shale	0.75	0.10	0.64	-29.8	-1.1	-5.5	1.35	2.71	9.2	-	-	-
67.32	Shale	0.76	0.03	0.72	-29.8	-1.0	-5.8	0.88	1.77	12.9	-	-	-
67.42	Shale	1.07	0.24	0.83	-29.5	-1.0	-6.2	0.28	0.56	27.4	3.6	0.051	16.43
67.51	Shale	1.03	0.28	0.75	-29.4	-1.1	-6.3	0.88	1.76	23.3	3.8	0.047	16.08
67.61	Shale	0.74	0.06	0.69	-29.7	-1.1	-6.6	0.22	0.44	8.3	4.2	0.049	13.98

67.72	Shale	0.75	0.02	0.72	-30.0	-1.0	-6.2	0.83	1.66	11.9	3.8	0.065	11.22
67.83	Shale	0.73	0.13	0.61	-29.8	-1.0	-6.1	0.94	1.89	14.3	3.9	0.061	9.90
67.93	Shale	0.73	0.10	0.63	-29.8	-1.4	-6.4	0.79	1.58	-	3.7	0.069	9.12
68.02	Shale	0.67	0.04	0.63	-29.4	-0.8	-5.7	2.08	4.17	6.3	4.2	0.065	9.73
68.12	Shale	0.75	0.05	0.71	-30.0	-1.1	-6.1	1.05	2.11	1.6	3.7	0.069	10.28
68.22	Shale	2.57	1.67	0.90	-29.3	-1.5	-5.9	0.55	1.10	4.4	4.7	0.033	27.67
68.33	Shale	1.19	0.33	0.86	-29.6	-1.2	-5.9	0.97	1.94	-11.7	4.0	0.063	13.59
68.41	Shale	0.91	0.08	0.84	-29.9	-0.8	-6.0	0.67	1.35	-1.1	3.8	0.067	12.52
68.53	Shale	0.86	0.04	0.82	-29.4	-0.6	-6.0	0.83	1.65	1.3	4.1	0.067	12.18
68.62	Shale	1.43	0.45	0.98	-29.5	-1.3	-6.1	0.80	1.60	0.7	4.2	0.054	17.93
68.72	Mix	4.49	2.52	1.98	-29.9	-1.0	-5.4	0.62	1.24	-16.1	4.5	0.045	43.79
68.80	Limestone	7.48	7.02	0.46	-30.0	-1.0	-4.5	0.42	0.85	-3.6	4.9	0.019	24.00
68.91	Shale	0.68	0.04	0.64	-29.6	-1.4	-4.6	0.75	1.50	-9.1	4.0	0.063	10.05
69.03	Shale	0.58	0.07	0.51	-29.7	-1.3	-6.7	0.65	1.31	-2.2	3.9	0.062	8.13
69.12	Shale	0.89	0.11	0.78	-29.7	-1.5	-6.4	0.72	1.44	9.9	4.0	0.050	15.74
69.20	Shale	0.51	0.04	0.47	-29.6	-1.2	-6.4	0.49	0.99	-1.3	3.4	0.067	6.94
69.33	Shale	0.44	0.01	0.42	-30.2	-1.5	-6.5	0.74	1.48	16.5	4.3	0.066	6.40
69.41	Shale	0.61	0.09	0.52	-29.7	-1.1	-6.4	0.50	1.00	6.6	4.7	0.055	9.42
69.50	Shale	0.69	0.04	0.66	-30.0	-1.4	-6.3	0.66	1.32	-9.1	4.1	0.068	9.68
69.61	Shale	1.05	0.60	0.44	-29.4	-1.8	-6.7	0.56	1.11	2.0	4.5	0.035	12.82
69.70	Shale	0.44	0.03	0.41	-29.9	-1.2	-5.8	0.91	1.81	2.1	4.1	0.071	5.78
69.82	Shale	0.69	0.05	0.64	-29.8	-1.1	-6.3	0.39	0.77	7.2	3.8	0.055	11.62
70.02	Shale	0.37	0.02	0.35	-29.5	-0.9	-6.6	0.66	1.33	-4.0	4.0	0.055	6.46
70.12	Limestone	3.47	3.34	0.13	-31.0	-1.6	-5.3	0.68	1.37	-11.9	3.8	0.058	2.23
70.22	Shale	0.57	0.12	0.45	-29.3	-0.9	-5.9	0.17	0.34	-4.4	3.4	0.053	8.59
70.32	Shale	0.75	0.07	0.68	-29.9	-0.6	-6.2	0.67	1.33	4.3	3.6	0.061	11.25

70.42	Mix	0.69	0.05	0.64	-30.0	-1.1	-6.7	0.82	1.64	-8.0	3.8	0.064	10.00
70.51	Shale	1.63	1.62	0.00	-30.0	-1.3	-5.9	1.09	2.19	-10.6	3.4	0.062	0.04
70.63	Shale	1.53	0.48	1.05	-29.3	-1.7	-6.4	0.16	0.31	-2.2	4.2	0.034	30.58
70.73	Shale	0.92	0.07	0.84	-29.7	-1.5	-6.5	0.95	1.89	-	3.7	0.046	18.30
70.83	Shale	0.90	0.09	0.81	-29.5	-	-	0.18	0.37	9.8	3.6	0.044	18.49
70.92	Shale	0.74	0.11	0.62	-29.5	-1.1	-5.7	0.14	0.28	9.6	4.4	0.052	11.97
71.01	Shale	0.65	0.12	0.53	-29.8	-1.1	-6.2	0.77	1.54	-6.8	3.4	0.057	9.35
71.12	Shale	0.58	0.02	0.56	-29.6	-0.9	-6.2	0.43	0.86	-4.4	3.2	0.055	10.28
71.22	Limestone	7.26	7.08	0.17	-29.4	-2.0	-5.4	0.74	1.47	-	3.1	0.025	6.76
71.34	Limestone	10.67	10.13	0.54	-27.8	-0.6	-5.3	0.17	0.35	-	1.2	0.004	129.07
71.42	Limestone	8.40	7.55	0.85	-29.1	-1.2	-5.2	0.17	0.34	-	1.5	0.008	111.43
71.51	Limestone	11.52	11.34	0.18	-27.7	-0.6	-5.1	0.09	0.19	-	-	-	-
71.63	Shale	1.68	0.21	1.47	-30.3	-	-	1.16	2.31	-7.4	3.2	0.059	24.82
71.74	Shale	1.14	0.61	0.52	-28.3	-1.8	-6.7	0.87	1.75	17.1	3.5	0.031	16.64
71.83	Shale	0.50	0.06	0.45	-29.7	-1.2	-6.4	0.38	0.76	-7.5	3.3	0.061	7.28
71.93	Shale	6.44	5.74	0.71	-29.6	-	-	0.31	0.61	-1.3	2.2	0.030	23.41
72.03	Limestone	6.46	6.03	0.43	-29.4	-1.2	-5.9	0.55	1.10	-6.5	2.4	0.035	12.28
72.13	Shale	0.83	0.09	0.74	-29.9	-1.1	-5.3	1.28	2.56	-13.8	3.4	0.062	11.92
72.24	Mix	1.80	7.06	0.00	-29.0	-1.0	-6.3	1.07	2.15	-23.7	2.7	0.055	-
72.34	Shale	1.39	0.25	1.14	-29.9	-1.1	-6.4	1.31	2.61	-16.1	3.1	0.064	-
72.44	Shale	0.50	0.15	0.35	-29.6	-1.2	-6.0	0.90	1.80	-	3.4	0.057	6.12
72.53	Shale	0.64	0.04	0.60	-29.9	-1.2	-6.3	0.58	1.16	-2.3	3.2	0.061	9.95
72.63	Shale	0.41	0.04	0.37	-29.5	-1.3	-6.0	0.91	1.82	11.7	3.3	0.053	7.04
72.74	Shale	0.54	0.05	0.49	-29.6	-1.4	-5.9	0.42	0.85	17.6	3.0	0.055	8.82
72.85	Shale	0.57	0.06	0.52	-29.8	-1.2	-5.6	0.56	1.12	35.3	3.4	0.055	9.46
72.93	Shale	0.56	0.07	0.49	-30.0	-1.6	-6.0	0.26	0.51	4.4	2.8	0.057	8.62

73.04	Shale	0.55	0.07	0.48	-29.9	-1.4	-6.2	0.86	1.73	5.9	2.9	0.063	7.61
73.14	Shale	0.51	0.06	0.45	-30.3	-	-	0.48	0.95	-	2.7	0.055	8.11
73.23	Shale	2.30	1.26	1.04	-30.0	-1.9	-6.4	1.51	3.01	-7.5	2.5	0.056	18.45
73.34	Shale	0.65	0.17	0.49	-30.0	-1.3	-6.2	0.78	1.56	-7.0	3.1	0.056	8.76
73.43	Shale	1.01	0.08	0.92	-29.4	-1.1	-6.9	0.14	0.28	-9.8	2.6	0.032	28.68
73.53	Shale	0.99	0.28	0.70	-30.0	-1.1	-6.5	0.61	1.22	-13.6	2.9	0.047	14.83
73.63	Shale	0.83	0.46	0.37	-29.6	-1.0	-6.7	0.32	0.64	17.8	2.6	0.037	9.84
73.73	Shale	0.50	0.13	0.38	-29.3	-1.1	-6.2	0.22	0.45	30.5	2.8	0.052	7.28
73.84	Shale	0.59	0.10	0.48	-29.6	-1.4	-6.1	0.17	0.33	-7.0	2.3	0.041	11.95
73.94	Limestone	7.29	6.29	1.00	-29.7	-1.9	-6.0	0.35	0.70	-	2.4	0.015	66.95
74.02	Limestone	3.21	2.93	0.28	-30.7	-1.6	-5.4	0.78	1.57	-10.4	1.5	0.043	6.49
74.13	Shale	0.89	0.21	0.68	-29.4	-1.3	-5.4	0.45	0.90	-	1.8	0.035	19.41
74.22	Shale	0.64	0.09	0.55	-29.6	-0.9	-5.8	0.50	1.00	-	2.5	0.042	12.95
74.33	Shale	0.57	0.02	0.54	-30.0	-1.5	-6.8	0.95	1.90	12.1	2.3	0.047	11.48
74.42	Shale	0.91	0.14	0.77	-29.0	-1.0	-5.9	0.93	1.87	1.0	3.8	0.053	14.61
74.52	Mix	1.72	0.84	0.88	-29.6	-1.8	-6.2	1.30	2.61	1.1	3.8	0.055	16.08
74.62	Shale	0.66	0.06	0.60	-29.2	-1.1	-5.6	0.74	1.47	-4.1	3.6	0.059	10.19
74.72	Shale	0.59	0.05	0.53	-29.4	-1.1	-5.8	1.12	2.24	24.3	3.7	0.063	8.45
74.82	Shale	0.93	0.25	0.68	-28.7	-1.0	-6.5	0.47	0.95	12.6	4.0	0.050	13.78
74.92	Shale	1.05	0.30	0.75	-29.0	-1.4	-6.4	0.15	0.30	0.4	4.3	0.038	19.80
75.02	Shale	1.07	0.34	0.72	-28.7	-1.5	-6.3	1.10	2.19	12.5	3.9	0.036	19.75
75.12	Shale	0.77	0.14	0.63	-29.5	-1.5	-6.5	0.67	1.34	22.4	4.1	0.038	16.40
75.22	Shale	0.75	0.17	0.58	-29.8	-1.4	-6.1	2.24	4.48	28.9	3.7	0.056	10.31
75.32	Limestone	9.79	8.82	0.97	-29.3	-2.1	-5.4	0.96	1.92	15.5	3.8	0.015	63.33
75.42	Shale	1.12	0.56	0.56	-30.0	-1.6	-6.6	0.72	1.43	-7.0	4.3	0.040	13.97
75.52	Limestone	11.64	11.20	0.43	-27.8	-2.8	-5.9	0.24	0.48	18.1	-	-	-

75.62	Shale	1.25	0.23	1.01	-30.3	-0.9	-5.8	0.71	1.43	-8.7	3.8	0.060	17.03
75.72	Shale	0.79	0.11	0.69	-30.0	-0.9	-6.0	0.19	0.39	3.1	4.0	0.052	13.08
75.82	Shale	0.52	0.03	0.49	-30.2	-0.7	-5.9	0.18	0.35	-1.8	3.9	0.063	7.89
75.92	Shale	1.11	0.29	0.81	-29.8	-1.3	-6.5	1.04	2.07	-8.3	3.5	0.060	13.68
76.02	Shale	0.99	0.02	0.97	-29.1	-0.8	-5.1	0.94	1.88	-5.8	3.7	0.057	16.85
76.12	Shale	1.39	0.17	1.22	-30.1	-1.3	-6.0	1.20	2.39	-15.7	3.0	0.068	17.86
76.22	Limestone	5.68	3.85	1.83	-29.8	-	-	0.58	1.16	-15.8	1.5	0.032	58.01
76.32	Shale	0.54	0.06	0.47	-30.1	-1.2	-6.4	0.42	0.85	-6.9	3.6	0.062	7.64
76.42	Shale	0.59	0.04	0.55	-30.0	-1.3	-6.4	0.63	1.27	-14.0	3.3	0.065	8.52
76.52	Shale	0.82	0.14	0.69	-29.8	-1.5	-5.6	0.47	0.94	-7.4	4.0	0.057	12.14
76.62	Shale	0.93	0.14	0.78	-30.1	-1.0	-6.3	0.79	1.57	-6.1	3.8	0.061	12.77
76.72	Shale	1.82	0.44	1.38	-29.9	-1.1	-5.4	0.62	1.24	-11.7	3.7	0.060	23.17
76.82	Shale	2.28	0.64	1.65	-28.6	-1.7	-6.5	0.07	0.13	7.4	4.9	0.026	62.73
76.92	Shale	0.92	0.12	0.80	-29.7	-0.9	-5.8	0.31	0.62	1.6	3.9	0.058	13.90
77.02	Shale	1.78	0.43	1.36	-29.2	-1.6	-6.5	0.59	1.18	40.8	4.5	0.030	45.26
77.12	Shale	2.87	1.32	1.55	-28.8	-0.9	-5.8	0.49	0.99	27.7	4.2	0.031	49.66
77.22	Shale	0.87	0.17	0.70	-29.8	-1.1	-6.0	0.35	0.69	2.5	3.8	0.053	13.25
77.32	Shale	0.90	0.17	0.72	-29.4	-1.0	-5.8	0.43	0.86	6.4	3.6	0.056	12.85
77.42	Shale	0.68	0.13	0.55	-30.2	-1.1	-6.1	0.46	0.91	7.2	3.6	0.060	9.30
77.52	Shale	0.74	0.08	0.66	-29.5	-1.1	-5.7	0.35	0.69	-1.7	3.7	0.056	11.78
77.62	Shale	2.44	1.46	0.98	-28.7	-1.4	-6.0	1.26	2.51	32.5	4.2	0.031	31.37
77.72	Shale	0.89	0.14	0.75	-29.5	-1.2	-6.0	0.33	0.65	0.0	4.1	0.051	14.57
77.82	Shale	0.66	0.08	0.58	-29.7	-1.1	-6.0	0.32	0.64	-3.4	5.3	0.056	10.33
77.92	Shale	1.30	0.51	0.80	-29.8	-1.2	-5.9	0.59	1.18	-4.8	5.2	0.053	15.14
78.02	Shale	0.99	0.15	0.85	-30.0	-1.3	-6.0	0.45	0.89	4.8	4.9	0.056	15.23
78.12	Shale	1.50	0.31	1.19	-29.3	-1.2	-5.9	0.24	0.48	1.2	5.6	0.045	-

78.22	Shale	1.30	0.49	0.81	-29.7	-1.3	-5.9	0.42	0.83	-6.0	5.8	0.054	14.86
78.32	Shale	0.94	0.21	0.73	-29.7	-1.2	-6.1	0.31	0.62	7.9	5.9	0.056	13.11
78.42	Shale	0.76	0.06	0.70	-29.4	-1.3	-5.7	0.18	0.36	19.9	5.6	0.056	12.43
78.52	Shale	1.02	0.29	0.72	-29.9	-1.2	-6.2	0.39	0.78	-2.7	5.1	0.059	12.33
78.62	Shale	1.44	1.15	0.30	-28.8	-1.4	-6.1	0.42	0.84	15.9	5.9	0.040	7.50

Appendix B

Depth (m)	Lithology	Fe _{carb} wt%	Fe _{oxide} wt%	Fe _{mag} wt%	Fe _{pyrite} wt%	Fe _{HR} wt%	Fe _{HR} /Fe _T wt%	Fe _{py} /Fe _{HR} wt%	Fe _{Unreactive} wt%	Fe _T wt%	P wt %	Al wt%
65.61	Mix	0.59	0.12	0.10	0.57	1.38	0.37	0.41	2.36	3.74	0.16	4.70
65.71	Limestone	0.34	0.01	0.00	0.06	0.41	0.69	0.15	0.18	0.59	0.04	0.17
65.80	Shale	0.41	0.14	0.30	0.55	1.39	0.28	0.40	3.64	5.04	0.14	7.01
65.91	Shale	0.60	0.14	0.30	0.79	1.82	0.46	0.43	2.16	3.99	0.18	5.01
66.02	Shale	0.53	0.11	0.13	0.33	1.10	0.40	0.30	1.65	2.75	0.13	3.28
66.11	Shale	0.34	0.16	0.30	0.40	1.19	0.24	0.33	3.77	4.96	0.13	8.29
66.23	Shale	0.38	0.13	0.26	0.22	0.99	0.22	0.22	3.42	4.40	0.13	7.33
66.33	Shale	0.44	0.12	0.23	0.08	0.87	0.25	0.09	2.65	3.52	0.15	5.70
66.42	Shale	0.33	0.16	0.31	0.34	1.14	0.24	0.30	3.63	4.77	0.13	8.15
66.52	Shale	0.35	0.15	0.31	0.75	1.56	0.37	0.48	2.67	4.22	0.20	6.31
66.61	Shale	0.33	0.12	0.27	0.32	1.04	0.22	0.31	3.60	4.64	0.17	6.72
66.72	Shale	0.34	0.15	0.28	0.42	1.18	0.24	0.35	3.67	4.85	0.15	8.12
66.82	Shale	0.29	0.14	0.26	0.53	1.22	0.26	0.43	3.54	4.76	0.14	8.02
66.92	Limestone	0.48	0.11	0.06	0.35	1.00	0.44	0.35	1.29	2.29	0.08	2.94
67.02	Limestone	0.65	0.16	0.14	0.57	1.52	0.47	0.37	1.71	3.24	0.16	3.85
67.12	Mix	0.50	0.10	0.03	0.42	1.06	0.50	0.40	1.08	2.14	0.07	2.47
67.22	Shale	0.31	0.16	0.24	1.18	1.89	0.40	0.62	2.78	4.67	0.15	8.00
67.32	Shale	0.31	0.14	0.25	0.77	1.47	0.34	0.52	2.86	4.33	0.12	7.79
67.42	Shale	0.39	0.15	0.28	0.24	1.06	0.24	0.23	3.35	4.42	0.15	6.82
67.51	Shale	0.36	0.13	0.25	0.77	1.51	0.36	0.51	2.67	4.18	0.15	6.61
67.61	Shale	0.30	0.14	0.26	0.19	0.89	0.21	0.21	3.45	4.34	0.14	6.92
67.72	Shale	0.29	0.18	0.30	0.72	1.49	0.30	0.49	3.43	4.92	0.12	7.85

67.83	Shale	0.25	0.14	0.24	0.82	1.45	0.31	0.57	3.29	4.74	0.12	8.08
67.93	Shale	0.23	0.11	0.23	0.69	1.25	0.28	0.55	3.18	4.44	0.11	8.25
68.02	Shale	0.27	0.19	0.23	1.81	2.51	0.56	0.72	1.96	4.47	0.11	7.81
68.12	Shale	0.25	0.13	0.22	0.92	1.52	0.33	0.60	3.05	4.58	0.10	7.99
68.22	Shale	0.47	0.12	0.19	0.48	1.26	0.40	0.38	1.88	3.14	-	-
68.33	Shale	0.30	0.14	0.24	0.85	1.52	0.35	0.56	2.81	4.33	0.12	7.35
68.41	Shale	0.33	0.14	0.27	0.59	1.32	0.30	0.44	3.04	4.36	0.12	7.77
68.53	Shale	0.31	0.15	0.24	0.72	1.41	0.33	0.51	2.91	4.32	0.12	7.70
68.62	Shale	0.44	0.15	0.26	0.70	1.55	0.39	0.45	2.38	3.94	0.15	6.43
68.72	Mix	0.57	0.12	0.15	0.54	1.38	0.44	0.39	1.73	3.11	0.13	4.93
68.80	Limestone	0.58	0.10	0.10	0.37	1.15	0.55	0.32	0.95	2.10	0.11	3.70
68.91	Shale	0.25	0.11	0.26	0.65	1.27	0.32	0.52	2.73	4.00	0.11	7.14
69.03	Shale	0.31	0.15	0.30	0.57	1.33	0.27	0.43	3.54	4.87	0.09	6.81
69.12	Shale	0.36	0.16	0.29	0.62	1.43	0.32	0.44	3.00	4.43	0.13	5.65
69.20	Shale	0.38	0.18	0.33	0.43	1.32	0.32	0.32	2.86	4.18	0.09	7.51
69.33	Shale	0.35	0.18	0.34	0.64	1.51	0.31	0.43	3.38	4.89	0.08	8.01
69.41	Shale	0.36	0.16	0.32	0.43	1.28	0.30	0.34	3.04	4.31	0.11	6.74
69.50	Shale	0.31	0.17	0.26	0.57	1.32	0.29	0.44	3.30	4.62	0.07	7.08
69.61	Shale	0.37	0.12	0.22	0.49	1.19	0.34	0.41	2.35	3.55	0.15	4.32
69.70	Shale	0.30	0.20	0.27	0.79	1.56	0.36	0.51	2.73	4.29	0.08	7.64
69.82	Shale	0.30	0.13	0.27	0.34	1.04	0.25	0.32	3.21	4.26	0.13	6.51
70.02	Shale	0.31	0.08	0.24	0.58	1.22	0.25	0.47	3.57	4.79	0.09	7.17
70.12	Limestone	0.39	0.13	0.16	0.59	1.27	0.30	0.47	2.97	4.24	0.08	5.06
70.22	Shale	0.33	0.08	0.26	0.15	0.82	0.19	0.18	3.61	4.43	0.11	7.21
70.32	Shale	0.33	0.08	0.25	0.58	1.24	0.23	0.47	4.05	5.30	0.12	7.60
70.42	Mix	0.30	0.13	0.26	0.71	1.40	0.24	0.51	4.35	5.75	0.13	7.77

70.51	Shale	0.39	0.12	0.21	0.95	1.67	0.33	0.57	3.40	5.07	0.12	6.86
70.63	Shale	0.48	0.06	0.21	0.14	0.89	0.23	0.15	2.92	3.80	0.15	4.54
70.73	Shale	0.41	0.08	0.23	0.82	1.55	0.37	0.53	2.59	4.14	0.12	6.15
70.83	Shale	0.39	0.05	0.25	0.16	0.85	0.20	0.19	3.49	4.33	0.12	6.01
70.92	Shale	0.41	0.04	0.25	0.12	0.83	0.18	0.15	3.89	4.72	0.09	7.35
71.01	Shale	0.31	0.03	0.28	0.67	1.30	0.29	0.52	3.21	4.51	0.13	7.23
71.12	Shale	0.33	0.02	0.25	0.37	0.98	0.21	0.38	3.58	4.56	0.10	7.23
71.22	Limestone	0.63	0.02	0.09	0.64	1.38	0.51	0.46	1.32	2.70	0.07	2.67
71.34	Limestone	0.51	0.01	0.02	0.15	0.68	0.71	0.22	0.28	0.96	0.03	0.60
71.42	Limestone	0.92	0.03	0.06	0.15	1.16	0.52	0.13	1.05	2.21	0.04	1.60
71.51	Limestone	0.66	0.00	0.01	0.08	0.75	0.90	0.11	0.09	0.83	0.02	0.26
71.63	Shale	0.34	0.14	0.18	1.01	1.67	0.38	0.60	2.73	4.40	0.11	6.20
71.74	Shale	0.66	0.16	0.24	0.76	1.82	0.43	0.42	2.44	4.26	0.11	4.85
71.83	Shale	0.26	0.09	0.28	0.33	0.96	0.19	0.35	4.00	4.96	0.08	7.44
71.93	Shale	2.30	0.19	0.09	0.27	2.85	0.64	0.09	1.61	4.46	0.06	2.91
72.03	Limestone	0.57	0.07	0.11	0.48	1.23	0.44	0.39	1.53	2.76	0.11	3.40
72.13	Shale	0.29	0.09	0.23	1.11	1.72	0.39	0.65	2.68	4.41	0.11	8.02
72.24	Mix	0.32	0.06	0.18	0.93	1.49	0.33	0.63	3.08	4.58	0.07	6.69
72.34	Shale	0.32	0.09	0.22	1.14	1.77	0.37	0.64	3.06	4.83	0.08	7.19
72.44	Shale	0.26	0.08	0.27	0.78	1.39	0.29	0.56	3.48	4.87	0.11	7.61
72.53	Shale	0.29	0.09	0.26	0.50	1.15	0.23	0.44	3.84	4.99	0.07	7.81
72.63	Shale	0.27	0.07	0.23	0.79	1.35	0.28	0.59	3.45	4.80	0.08	7.07
72.74	Shale	0.30	0.08	0.26	0.37	1.01	0.19	0.37	4.42	5.42	0.08	6.66
72.85	Shale	0.43	0.08	0.31	0.49	1.31	0.27	0.37	3.49	4.79	0.09	7.48
72.93	Shale	0.29	0.06	0.22	0.22	0.80	0.15	0.28	4.38	5.17	0.08	7.48
73.04	Shale	0.36	0.04	0.26	0.75	1.41	0.26	0.53	3.91	5.32	0.06	7.80

73.14	Shale	0.32	0.03	0.26	0.41	1.02	0.20	0.41	3.99	5.01	0.08	6.02
73.23	Shale	0.39	0.02	0.16	1.31	1.88	0.41	0.70	2.66	4.54		
73.34	Shale	0.35	0.02	0.28	0.68	1.33	0.28	0.51	3.37	4.70	0.08	7.68
73.43	Shale	0.35	0.00	0.22	0.12	0.70	0.17	0.17	3.33	4.03	0.13	5.18
73.53	Shale	0.27	0.01	0.25	0.53	1.06	0.23	0.50	3.63	4.70	0.08	7.09
73.63	Shale	0.30	0.00	0.24	0.28	0.81	0.20	0.34	3.25	4.06	0.11	5.97
73.73	Shale	0.41	0.01	0.29	0.20	0.90	0.17	0.22	4.31	5.21	0.08	8.25
73.84	Shale	0.30	0.00	0.26	0.15	0.70	0.15	0.21	3.98	4.68	0.09	6.62
73.94	Limestone	0.69	0.01	0.11	0.30	1.12	0.42	0.27	1.53	2.65	0.10	2.81
74.02	Limestone	0.58	0.01	0.19	0.68	1.46	0.35	0.47	2.66	4.12	0.15	6.25
74.13	Shale	0.47	0.01	0.31	0.39	1.19	0.25	0.33	3.53	4.72	0.14	6.57
74.22	Shale	0.27	0.00	0.25	0.43	0.95	0.20	0.45	3.78	4.73	0.07	7.38
74.33	Shale	0.25	0.06	0.28	0.83	1.43	0.28	0.58	3.63	5.05	0.10	7.33
74.42	Shale	0.20	0.12	0.13	0.81	1.26	0.27	0.65	3.45	4.71	0.07	6.16
74.52	Mix	0.35	0.10	0.15	1.13	1.74	0.39	0.65	2.67	4.40	0.09	6.47
74.62	Shale	0.25	0.11	0.14	0.64	1.14	0.22	0.56	4.07	5.22	0.07	7.22
74.72	Shale	0.27	0.10	0.17	0.97	1.52	0.30	0.64	3.61	5.13	0.07	7.70
74.82	Shale	0.34	0.09	0.16	0.41	1.01	0.21	0.41	3.74	4.74	0.09	6.26
74.92	Shale	0.43	0.10	0.17	0.13	0.83	0.20	0.16	3.31	4.15	0.11	5.06
75.02	Shale	0.40	0.12	0.17	0.95	1.65	0.39	0.58	2.58	4.23	0.11	4.75
75.12	Shale	0.36	0.12	0.19	0.58	1.26	0.29	0.46	3.09	4.34	0.10	4.89
75.22	Shale	0.28	0.19	0.17	1.95	2.58	0.51	0.76	2.51	5.10	0.08	6.44
75.32	Limestone	0.62	0.14	0.02	0.84	1.61	0.75	0.52	0.54	2.16	0.05	1.71
75.42	Shale	0.36	0.11	0.15	0.62	1.24	0.28	0.50	3.15	4.39	0.12	5.17
75.52	Limestone	0.48	0.02	0.01	0.21	0.72	0.85	0.29	0.13	0.85	0.03	0.39
75.62	Shale	0.34	0.12	0.17	0.62	1.24	0.26	0.50	3.63	4.88	0.13	6.75

75.72	Shale	0.34	0.10	0.15	0.17	0.77	0.16	0.22	3.99	4.76	0.09	6.39
75.82	Shale	0.28	0.11	0.13	0.15	0.67	0.13	0.23	4.54	5.22	0.07	7.79
75.92	Shale	0.27	0.11	0.16	0.90	1.44	0.29	0.63	3.53	4.97	0.09	6.87
76.02	Shale	0.29	0.11	0.16	0.82	1.38	0.29	0.59	3.44	4.82	0.10	6.75
76.12	Shale	0.26	0.12	0.14	1.04	1.56	0.33	0.67	3.18	4.74	0.14	6.83
76.22	Limestone	0.54	0.10	0.07	0.51	1.22	0.35	0.42	2.30	3.52	0.09	3.75
76.32	Shale	0.22	0.09	0.12	0.37	0.81	0.16	0.46	4.09	4.90	0.07	7.06
76.42	Shale	0.22	0.10	0.12	0.55	0.99	0.20	0.56	4.05	5.04	0.06	7.40
76.52	Shale	0.27	0.07	0.18	0.41	0.94	0.20	0.44	3.78	4.72	0.07	6.93
76.62	Shale	0.29	0.07	0.16	0.68	1.21	0.24	0.56	3.76	4.98	0.09	7.07
76.72	Shale	0.36	0.08	0.15	0.54	1.13	0.23	0.48	3.72	4.85	0.11	6.69
76.82	Shale	0.69	0.06	0.16	0.06	0.97	0.27	0.06	2.69	3.66	0.13	3.82
76.92	Shale	0.36	0.06	0.17	0.27	0.87	0.17	0.31	4.26	5.13	0.07	7.51
77.02	Shale	0.61	0.10	0.19	0.51	1.42	0.36	0.36	2.51	3.92	0.12	4.33
77.12	Shale	0.44	0.09	0.16	0.43	1.12	0.31	0.39	2.50	3.61	0.10	4.37
77.22	Shale	0.36	0.06	0.19	0.30	0.91	0.19	0.33	3.87	4.78	0.09	6.94
77.32	Shale	0.34	0.05	0.20	0.37	0.96	0.21	0.39	3.58	4.54	0.08	6.58
77.42	Shale	0.29	0.04	0.19	0.40	0.92	0.18	0.43	4.30	5.22	0.08	7.73
77.52	Shale	0.31	0.11	0.22	0.30	0.95	0.19	0.32	3.94	4.89	0.08	7.29
77.62	Shale	0.53	0.10	0.17	1.09	1.89	0.42	0.58	2.57	4.45	0.13	4.24
77.72	Shale	0.34	0.10	0.17	0.28	0.90	0.20	0.32	3.57	4.46	0.09	6.62
77.82	Shale	0.29	0.10	0.19	0.28	0.85	0.17	0.33	4.01	4.86	0.08	7.35
77.92	Shale	0.33	0.09	0.17	0.48	1.07	0.23	0.45	3.56	4.63	0.08	6.51
78.02	Shale	0.31	0.10	0.20	0.39	0.99	0.20	0.39	3.93	4.92	0.09	7.16
78.12	Shale	0.40	0.09	0.18	0.21	0.88	0.20	0.24	3.53	4.41	0.10	6.24
78.22	Shale	0.32	0.09	0.18	0.36	0.96	0.20	0.38	3.78	4.73	0.09	6.80

78.32	Shale	0.29	0.09	0.20	0.27	0.85	0.17	0.32	4.20	5.06	0.08	7.50
78.42	Shale	0.27	0.09	0.22	0.16	0.74	0.15	0.21	4.32	5.05	0.11	7.43
78.52	Shale	0.32	0.09	0.20	0.34	0.95	0.19	0.36	3.93	4.87	0.08	7.39
78.62	Shale	0.36	0.10	0.21	0.36	1.04	0.23	0.35	3.39	4.44	0.12	5.82

REFERENCES

- Ader, M., Thomazo, C., Sansjofre, P., Busigny, V., Papineau, D., Laffont, R., ... & Halverson, G. P. (2016). Interpretation of the nitrogen isotopic composition of Precambrian sedimentary rocks: Assumptions and perspectives. *Chemical Geology*, 429, 93-110.
- Algeo, T. J., Heckel, P. H., Maynard, J. B., Blakey, R., Rowe, H., Pratt, B. R., & Holmden, C. (2008). Modern and ancient epeiric seas and the super-estuarine circulation model of marine anoxia. *Dynamics of Epeiric seas: sedimentological, paleontological and geochemical perspectives*. St. John's, Canada: Geological Association of Canada, Special Publication, 48, 7-38.
- Baird, G. C., & Brett, C. E. (2002). Indian Castle Shale: late synorogenic siliciclastic succession in an evolving Middle to Late Ordovician foreland basin, eastern New York State. *Physics and Chemistry of the Earth, parts A/B/C*, 27(1-3), 203-230.
- Bergström, S. M., Young, S., & Schmitz, B. (2010). Katian (Upper Ordovician) $\delta^{13}\text{C}$ chemostratigraphy and sequence stratigraphy in the United States and Baltoscandia: A regional comparison. *Palaeogeography, Palaeoclimatology, Palaeoecology*, 296(3-4), 217-234.
- Berman-Frank, I., Quigg, A., Finkel, Z. V., Irwin, A. J., & Haramaty, L. (2007). Nitrogen-fixation strategies and Fe requirements in cyanobacteria. *Limnology and Oceanography*, 52(5), 2260-2269.
- Berner, R. A. (1991). A model for atmospheric CO₂ over phanerozoic time. *American Journal of Science*; (United States), 291(4).

- Berner, R. A. (1994). GEOCARB II: A revised model of atmospheric CO₂ over phanerozoic time. *American Journal of Science*; (United States), 294(1).
- Bond, D. P., & Grasby, S. E. (2020). Late Ordovician mass extinction caused by volcanism, warming, and anoxia, not cooling and glaciation. *Geology*.
- Bottjer, D. J., Droser, M. L., Sheehan, P. M., McGhee, G. R., & Allmon, W. D. (2001). The ecological architecture of major events in the Phanerozoic history of marine invertebrate life. *Evolutionary paleoecology*. Columbia University Press, New York, 35-61.
- Boudou, J. P., Schimmelmann, A., Ader, M., Mastalerz, M., Sebiló, M., & Gengembre, L. (2008). Organic nitrogen chemistry during low-grade metamorphism. *Geochimica et Cosmochimica Acta*, 72(4), 1199-1221.
- Brenchley, P. (1984). Later Ordovician extinction and their relationship to the Gondwana glaciation. *Fossil and Climate*.
- Brenchley, P. J., Marshall, J. D., Carden, G. A. F., Robertson, D. B. R., Long, D. G. F., Meidla, T., ... & Anderson, T. F. (1994). Bathymetric and isotopic evidence for a short-lived Late Ordovician glaciation in a greenhouse period. *Geology*, 22(4), 295-298.
- Brenchley, P. J., Carden, G. A., Hints, L., Kaljo, D., Marshall, J. D., Martma, T., ... & Nölvak, J. (2003). High-resolution stable isotope stratigraphy of Upper Ordovician sequences: Constraints on the timing of bioevents and environmental changes associated with mass extinction and glaciation. *Geological Society of America Bulletin*, 115(1), 89-104.

- Brett, C. E., Aucoin, C. D., Dattilo, B. F., Freeman, R. L., Hartshorn, K. R., McLaughlin, P. I., & Schwalbach, C. E. (2020). Revised sequence stratigraphy of the upper Katian Stage (Cincinnatian) strata in the Cincinnati Arch reference area: geological and paleontological implications. *Palaeogeography, Palaeoclimatology, Palaeoecology*, 540, 109483.
- Brett, C. E., & Algeo, T. J. (2001). Sequence stratigraphy of Upper Ordovician and Lower Silurian strata of the Cincinnati Arch region. In *Sequence, Cycle and Event Stratigraphy of Upper Ordovician & Silurian Strata of the Cincinnati Arch Region*: SEPM, Great Lakes Section, 1999 Field Conference Guidebook (pp. 34-46).
- Brett, C. E., Algeo, T. J., & McLaughlin, P. I. (2008)a. Use of event beds and sedimentary cycles in high-resolution stratigraphic correlation of lithologically repetitive successions. In *High-Resolution Approaches in Stratigraphic Paleontology* (pp. 315-350). Springer, Dordrecht.
- Brett, C. E., Kirchner, B. T., Tsujita, C. J., Dattilo, B. F., Pratt, B. R., & Holmden, C. (2008)b. Depositional dynamics recorded in mixed siliciclastic-carbonate marine successions: Insights from the Upper Ordovician Kope Formation of Ohio and Kentucky, USA. *Dynamics of Epeiric Seas: Geological Association of Canada Special Paper*, 48, 73-102.
- Buggisch, W., Joachimski, M. M., Lehnert, O., Bergström, S. M., Repetski, J. E., & Webers, G. F. (2010). Did intense volcanism trigger the first Late Ordovician icehouse?. *Geology*, 38(4), 327-330.

- Canfield, D. E., Raiswell, R., Westrich, J. T., Reaves, C. M., & Berner, R. A. (1986). The use of chromium reduction in the analysis of reduced inorganic sulfur in sediments and shales. *Chemical geology*, 54(1-2), 149-155.
- Cline, J. D. (1969). Spectrophotometric determination of hydrogen sulfide in natural waters 1. *Limnology and Oceanography*, 14(3), 454-458.
- Cocks, L. R. M., & Torsvik, T. H. (2011). The Palaeozoic geography of Laurentia and western Laurussia: a stable craton with mobile margins. *Earth-Science Reviews*, 106(1-2), 1-51.
- Coleman, M. L. (1985). Geochemistry of diagenetic non-silicate minerals: kinetic considerations. *Philosophical Transactions of the Royal Society of London. Series A, Mathematical and Physical Sciences*, 315(1531), 39-56.
- Daniels, E. J., & Altaner, S. P. (1990). Clay mineral authigenesis in coal and shale from the Anthracite region, Pennsylvania. *American Mineralogist*, 75(7-8), 825-839.
- Dattilo, B. F., Brett, C. E., Tsujita, C. J., & Fairhurst, R. (2008). Sediment supply versus storm winnowing in the development of muddy and shelly interbeds from the Upper Ordovician of the Cincinnati region, USA. *Canadian Journal of Earth Sciences*, 45(2), 243-265.
- Delwiche, C. C., & Steyn, P. L. (1970). Nitrogen isotope fractionation in soils and microbial reactions. *Environmental Science & Technology*, 4(11), 929-935.
- Devol, A. H. (2008). Denitrification including anammox. *Nitrogen in the marine environment*, 2, 263-301.

- Edwards, C. T., & Saltzman, M. R. (2014). Carbon isotope ($\delta^{13}\text{C}_{\text{carb}}$) stratigraphy of the Lower–Middle Ordovician (Tremadocian–Darriwilian) in the Great Basin, western United States: implications for global correlation. *Palaeogeography, Palaeoclimatology, Palaeoecology*, 399, 1-20.
- Edwards, C. T., Saltzman, M. R., Royer, D. L., & Fike, D. A. (2017). Oxygenation as a driver of the Great Ordovician Biodiversification Event. *Nature Geoscience*, 10(12), 925-929.
- Ellwood, B. B., Brett, C. E., & MacDonald, W. D. (2007). Magnetostratigraphy susceptibility of the Upper Ordovician Kope Formation, northern Kentucky. *Palaeogeography, Palaeoclimatology, Palaeoecology*, 243(1-2), 42-54.
- Farrell, Ú. C., Briggs, D. E., Hammarlund, E. U., Sperling, E. A., & Gaines, R. R. (2013). Paleoredox and pyritization of soft-bodied fossils in the Ordovician Frankfort Shale of New York. *American Journal of Science*, 313(5), 452-489.
- Finney, S. C., Berry, W. B., Cooper, J. D., Ripperdan, R. L., Sweet, W. C., Jacobson, S. R., ... & Noble, P. J. (1999). Late Ordovician mass extinction: A new perspective from stratigraphic sections in central Nevada. *Geology*, 27(3), 215-218.
- Fraga-Ferreira, P. L., Ader, M., Caetano-Filho, S., Sansjofre, P., Paula-Santos, G. M., Babinski, M., ... & Trindade, R. I. (2021). The Nitrogen Cycle in an Epeiric Sea in the Core of Gondwana Supercontinent: A Study on the Ediacaran-Cambrian Bambui Group, East-central Brazil. *Frontiers in Earth Science*, 678.
- Gruber, N. (2008). The marine nitrogen cycle: overview and challenges. *Nitrogen in the marine environment*, 2, 1-50.

- Harper, D. A., Hammarlund, E. U., & Rasmussen, C. M. (2014). End Ordovician extinctions: a coincidence of causes. *Gondwana Research*, 25(4), 1294-1307.
- Holland, S. M., Meyer, D. L., & Miller, A. I. (2000). High-resolution correlation in apparently monotonous rocks: upper Ordovician Kope Formation, Cincinnati Arch. *Palaios*, 15(1), 73-80
- Holland, S. M., Miller, A. I., Meyer, D. L., & Dattilo, B. F. (2001). The detection and importance of subtle biofacies within a single lithofacies: the Upper Ordovician Kope Formation of the Cincinnati, Ohio region. *Palaios*, 16(3), 205-217.
- Holland, S. M., Miller, A. I., Dattilo, B. F., Meyer, D. L., & Diekmeyer, S. L. (1997). Cycle anatomy and variability in the storm-dominated type Cincinnati (Upper Ordovician): Coming to grips with cycle delineation and genesis. *The Journal of Geology*, 105(2), 135-152.
- IPCC (2014). *Climate Change 2014: Synthesis Report. Contribution of Working Groups I, II and III to the Fifth Assessment Report of the Intergovernmental Panel on Climate Change* [Core Writing Team, R.K. Pachauri and L.A. Meyer (eds.)]. IPCC, Geneva, Switzerland, 151 pp.
- Jablonski, D. (1991). Extinctions: a paleontological perspective. *Science*, 253(5021), 754-757.
- Jennette, D. C., & Pryor, W. A. (1993). Cyclic alteration of proximal and distal storm facies; Kope and Fairview formations (Upper Ordovician), Ohio and Kentucky. *Journal of Sedimentary Research*, 63(2), 183-203.

- Jin, J., Harper, D. A., Cocks, L. R. M., McCausland, P. J., Rasmussen, C. M., & Sheehan, P. M. (2013). Precisely locating the Ordovician equator in Laurentia. *Geology*, 41(2), 107-110.
- Jones, D. S., Fike, D. A., Finnegan, S., Fischer, W. W., Schrag, D. P., & McCay, D. (2011). Terminal Ordovician carbon isotope stratigraphy and glacioeustatic sea-level change across Anticosti Island (Québec, Canada). *Bulletin*, 123(7-8), 1645-1664.
- Kah, L. C., Lyons, T. W., & Frank, T. D. (2004). Low marine sulphate and protracted oxygenation of the Proterozoic biosphere. *Nature*, 431(7010), 834-838.
- Kampschulte, A., & Strauss, H. (2004). The sulfur isotopic evolution of Phanerozoic seawater based on the analysis of structurally substituted sulfate in carbonates. *Chemical Geology*, 204(3-4), 255-286.
- Kasting, J. F. (1992). Paradox lost and paradox found. *Nature*, 355(6362), 676-677.
- Kump, L. R., & Arthur, M. A. (1999). Interpreting carbon-isotope excursions: carbonates and organic matter. *Chemical Geology*, 161(1-3), 181-198.
- Kump, L. R., Arthur, M. A., Patzkowsky, M. E., Gibbs, M. T., Pinkus, D. S., & Sheehan, P. M. (1999). A weathering hypothesis for glaciation at high atmospheric pCO₂ during the Late Ordovician. *Palaeogeography, Palaeoclimatology, Palaeoecology*, 152(1-2), 173-187.
- Lehmann, M. F., Bernasconi, S. M., Barbieri, A., & McKenzie, J. A. (2002). Preservation of organic matter and alteration of its carbon and nitrogen isotope composition during simulated and in situ early sedimentary diagenesis. *Geochimica et Cosmochimica Acta*, 66(20), 3573-3584.

- Liu, X., Fike, D., Li, A., Dong, J., Xu, F., Zhuang, G., ... & Wan, S. (2019). Pyrite sulfur isotopes constrained by sedimentation rates: Evidence from sediments on the East China Sea inner shelf since the late Pleistocene. *Chemical Geology*, 505, 66-75.
- Luo, G., Algeo, T. J., Zhan, R., Yan, D., Huang, J., Liu, J., & Xie, S. (2016). Perturbation of the marine nitrogen cycle during the Late Ordovician glaciation and mass extinction. *Palaeogeography, Palaeoclimatology, Palaeoecology*, 448, 339-348.
- Marshall, N. T. (2011). Silt in the Upper Ordovician Kope Formation (Ohio, Indiana, Kentucky): The Enlightening Wildcard (Doctoral dissertation, University of Cincinnati).
- Meek, F.B. 1872: Descriptions of two new star-fishes, and a crinoid, from the Cincinnati Group of Ohio and Indiana. *American Journal of Science, Series 3*, vol. 3, p. 257–262.
- Melchin, M. J., Mitchell, C. E., Holmden, C., & Štorch, P. (2013). Environmental changes in the Late Ordovician–early Silurian: Review and new insights from black shales and nitrogen isotopes. *GSA Bulletin*, 125(11-12), 1635-1670.
- Miller, A. I., Holland, S. M., Dattilo, B. F., & Meyer, D. L. (1997). Stratigraphic resolution and perceptions of cycle architecture: Variations in meter-scale cyclicity in the type Cincinnati Series. *The Journal of Geology*, 105(6), 737-743.
- Miller, K. G., Kominz, M. A., Browning, J. V., Wright, J. D., Mountain, G. S., Katz, M. E., ... & Pekar, S. F. (2005). The Phanerozoic record of global sea-level change. *science*, 310(5752), 1293-1298.
- Newberry, J. S. (1871). *Geological Survey of Ohio*. Nevins & Myers, State Printers.

- Nieuwenhuize, J., Maas, Y. E., & Middelburg, J. J. (1994). Rapid analysis of organic carbon and nitrogen in particulate materials. *Marine Chemistry*, 45(3), 217-224.
- Oehlert, A. M., & Swart, P. K. (2014). Interpreting carbonate and organic carbon isotope covariance in the sedimentary record. *Nature Communications*, 5, 4672.
- Orazi, D.L., May J. I., Gilhooly III W.P., Dattilo B. F., (2017). A Combined Sedimentological and Multi-Proxy Geochemical Analysis of Southern Indiana Phosphate Rock. Butler University Undergraduate Research Conference.
- Pancost, R. D., Freeman, K. H., Herrmann, A. D., Patzkowsky, M. E., Ainsaar, L., & Martma, T. (2013). Reconstructing Late Ordovician carbon cycle variations. *Geochimica et Cosmochimica Acta*, 105, 433-454.
- Pasquier, V., Bryant, R. N., Fike, D. A., & Halevy, I. (2021). Strong local, not global, controls on marine pyrite sulfur isotopes. *Science advances*, 7(9), eabb7403.
- Pasquier, V., Sansjofre, P., Rabineau, M., Revillon, S., Houghton, J., & Fike, D. A. (2017). Pyrite sulfur isotopes reveal glacial– interglacial environmental changes. *Proceedings of the National Academy of Sciences*, 114(23), 5941-5945.
- Pellerin, A., Bui, T.H., Rough, M., Mucci, A., Canfield, D., & Wing, B. (2015). Mass-dependent sulfur isotope fractionation during reoxidative sulfur cycling: A case study from Mangrove Lake, Bermuda. *Geochimica Cosmochimica Acta*, 149, 152-164.
- Poulton, S. W., & Canfield, D. E. (2005). Development of a sequential extraction procedure for iron: implications for iron partitioning in continentally derived particulates. *Chemical Geology*, 214(3-4), 209-221.

- Poulton, S. W., & Canfield, D. E. (2011). Ferruginous conditions: a dominant feature of the ocean through Earth's history. *Elements*, 7(2), 107-112.
- Quan, T. M., Adigwe, E. N., Riedinger, N., & Puckette, J. (2013). Evaluating nitrogen isotopes as proxies for depositional environmental conditions in shales: Comparing Caney and Woodford Shales in the Arkoma Basin, Oklahoma. *Chemical Geology*, 360, 231-240.
- Quan, T. M., & Falkowski, P. G. (2009). Redox control of N: P ratios in aquatic ecosystems. *Geobiology*, 7(2), 124-139.
- Raiswell, R., Hardisty, D. S., Lyons, T. W., Canfield, D. E., Owens, J. D., Planavsky, N. J., ... & Reinhard, C. T. (2018). The iron paleoredox proxies: A guide to the pitfalls, problems and proper practice. *American Journal of Science*, 318(5), 491-526.
- Rasmussen, C. M., Kröger, B., Nielsen, M. L., & Colmenar, J. (2019). Cascading trend of Early Paleozoic marine radiations paused by Late Ordovician extinctions. *Proceedings of the National Academy of Sciences*, 116(15), 7207-7213.
- Reiners, P. W., & Turchyn, A. V. (2018). Extraterrestrial dust, the marine lithologic record, and global biogeochemical cycles. *Geology*, 46(10), 863-866.
- Richardson, J.A., Keating, C., Lepland, A., Hints, O., Bradley, A.S. and Fike, D.A. (2019). Silurian records of carbon and sulfur cycling from Estonia: The importance of depositional environment on isotopic trends. *Earth and Planetary Science Letters*, 512, pp.71-82.

- Robinson, R. S., Kienast, M., Luiza Albuquerque, A., Altabet, M., Contreras, S., De Pol Holz, R., ... & Ivanochko, T. (2012). A review of nitrogen isotopic alteration in marine sediments. *Paleoceanography*, 27(4).
- Sepkoski Jr, J. J. (1981). A factor analytic description of the Phanerozoic marine fossil record. *Paleobiology*, 36-53.
- Sepkoski, J. J. (1996). Patterns of Phanerozoic extinction: a perspective from global data bases. In *Global events and event stratigraphy in the Phanerozoic* (pp. 35-51). Springer, Berlin, Heidelberg.
- Servais, T., Owen, A. W., Harper, D. A., Kröger, B., & Munnecke, A. (2010). The great Ordovician biodiversification event (GOBE): the palaeoecological dimension. *Palaeogeography, Palaeoclimatology, Palaeoecology*, 294(3-4), 99-119.
- Schubert, C. J., & Calvert, S. E. (2001). Nitrogen and carbon isotopic composition of marine and terrestrial organic matter in Arctic Ocean sediments: implications for nutrient utilization and organic matter composition. *Deep Sea Research Part I: Oceanographic Research Papers*, 48(3), 789-810
- Sheehan, P. M. (2001). The late Ordovician mass extinction. *Annual Review of Earth and Planetary Sciences*, 29(1), 331-364.
- Shen, J., Pearson, A., Henkes, G. A., Zhang, Y. G., Chen, K., Li, D., ... & Shen, Y. (2018). Improved efficiency of the biological pump as a trigger for the Late Ordovician glaciation. *Nature Geoscience*, 11(7), 510
- Stigall, A. L. (2017). Ordovician oxygen and biodiversity. *Nature Geoscience*, 10(12), 887-888.

- Stigall, A. L., Freeman, R. L., Edwards, C. T., & Rasmussen, C. M. (2020). A multidisciplinary perspective on the Great Ordovician Biodiversification Event and the development of the early Paleozoic world. *Palaeogeography Palaeoclimatology Palaeoecology*, 543, 109521.
- Talbot, Michael R. "Nitrogen isotopes in palaeolimnology." *Tracking environmental change using lake sediments*. Springer, Dordrecht, 2002. 401-439.
- Volkova, I.B., Bogdanova, M.V., 1989. Properties of high-rank coals and dispersed organic matter of associated rocks in the Donets Basin (U.S.S.R.). *Int. J. Coal Geol.* 11, 315–339.
- Wada, E. (1980). Nitrogen isotope fractionation and its significance in biogeochemical processes occurring in marine environments. *Isotope marine chemistry*, 375-398.
- Webby, B. D., Paris, F., Droser, M. L., & Percival, I. G. (Eds.). (2012). *The great Ordovician biodiversification event*. Columbia University Press.
- Williams, L. B., Ferrell Jr, R. E., Hutcheon, I., Bakel, A. J., Walsh, M. M., & Krouse, H. R. (1995). Nitrogen isotope geochemistry of organic matter and minerals during diagenesis and hydrocarbon migration. *Geochimica et Cosmochimica Acta*, 59(4), 765-779.
- Young, S. A., Saltzman, M. R., Bergström, S. M., Leslie, S. A., & Xu, C. (2008). Paired $\delta^{13}\text{C}_{\text{carb}}$ and $\delta^{13}\text{C}_{\text{org}}$ records of Upper Ordovician (Sandbian–Katian) carbonates in North America and China: implications for paleoceanographic change. *Palaeogeography, Palaeoclimatology, Palaeoecology*, 270(1-2), 166-178.

Zou, C., Qiu, Z., Poulton, S. W., Dong, D., Wang, H., Chen, D., ... & Tao, H. (2018).

Ocean euxinia and climate change “double whammy” drove the Late Ordovician mass extinction. *Geology*, 46(6), 535-538.

CURRICULUM VITAE

Evelyn S Becerra

Education

- Master of Science in Geology, earned at Indiana University-Purdue University Indianapolis (IUPUI) September 2022
- Bachelor of Science in Geology, earned at the University of California, Riverside (UCR) July 2016

Professional Experience

- Teaching Assistant, IUPUI
 - August 2017- May 2019
- Lab Assistant, UCR Biogeochemistry Lab
 - November 2016- July 2017
- Lab Assistant, UCR Biogeochemistry Lab
 - October 2016- July 2017
- Undergraduate Lab Assistant, UCR Biogeochemistry Lab
 - April 2015- September 2016

Honors and Awards

- George Lapins Field Camp Departmental Scholarship, earned Spring 2016
- Dean's Honors List, earned Spring 2016
- Dean's Honors List, earned Fall 2015
- Women in Mining, California Chapter Scholarship, earned Spring 2014
- Los Angeles Basin Geological Society Scholarship, earned Spring 2014

Poster Presentations

- Midwest Geobiology Symposium, presented Fall 2018
- Geological Society of America (GSA) National Meeting, presented Fall 2018
- Crossroads Conference Indiana University, Bloomington, presented Spring 2019